Mechanical properties and machining of 3D printed composites

3.1 Introduction:

The objective of this chapter is to investigate the impact of the fibre filament fill pattern on the notch sensitivity of 3D printed CFRTs. In this chapter, FDM (Fused deposition modeling) 3D printing technology was used to create three different types of continuous fiber reinforced composites. and the reinforcements are glass fiber (GFRT), High strength high temperature fiber (HSHTFRT) and Kevlar fiber (KFRT), and a comprehensive study on their tensile properties, impact properties, flexural properties and machining such as material removal rate (MRR) In addition, failure behaviour was demonstrated. This chapter describe about the machining performance of three different 3D printed CFRTs composite materials (GFRT, HSHTFRT and KFRT) in terms of Material removal rate when slot micro-milling. Experimental design is performed using Taguchi's L_9 orthogonal array. A number of performance factors, including material removal rate, are taken into account while optimising machining process parameters including feed rate, tool cutting speed, cutting environment (dry), and depth of cut. The significant parameter are discovered using ANOVA and the regression analysis was done in order to investigate the deviation of result or to check the correctness of result. Specific surface area of material will describe the adsorbent property of material and it is calculated from thermogravimetric analysis (TGA). The thermal properties and flame retardancy of all the three different types of composite were investigated, and the possible flame retarding mechanism was proposed. The current study also looked at how the composites responded to low-velocity impacts based on ASTM specifications, where the v-

notch is used in order to evaluate the impact energy and impact resilience. The bonding strength and physical defects on the surface of composites and the failure behavior are characterized by using a scanning electron microscope (SEM) techniques.

3.2 Materials and composite fabrications

3.2.1 Material details

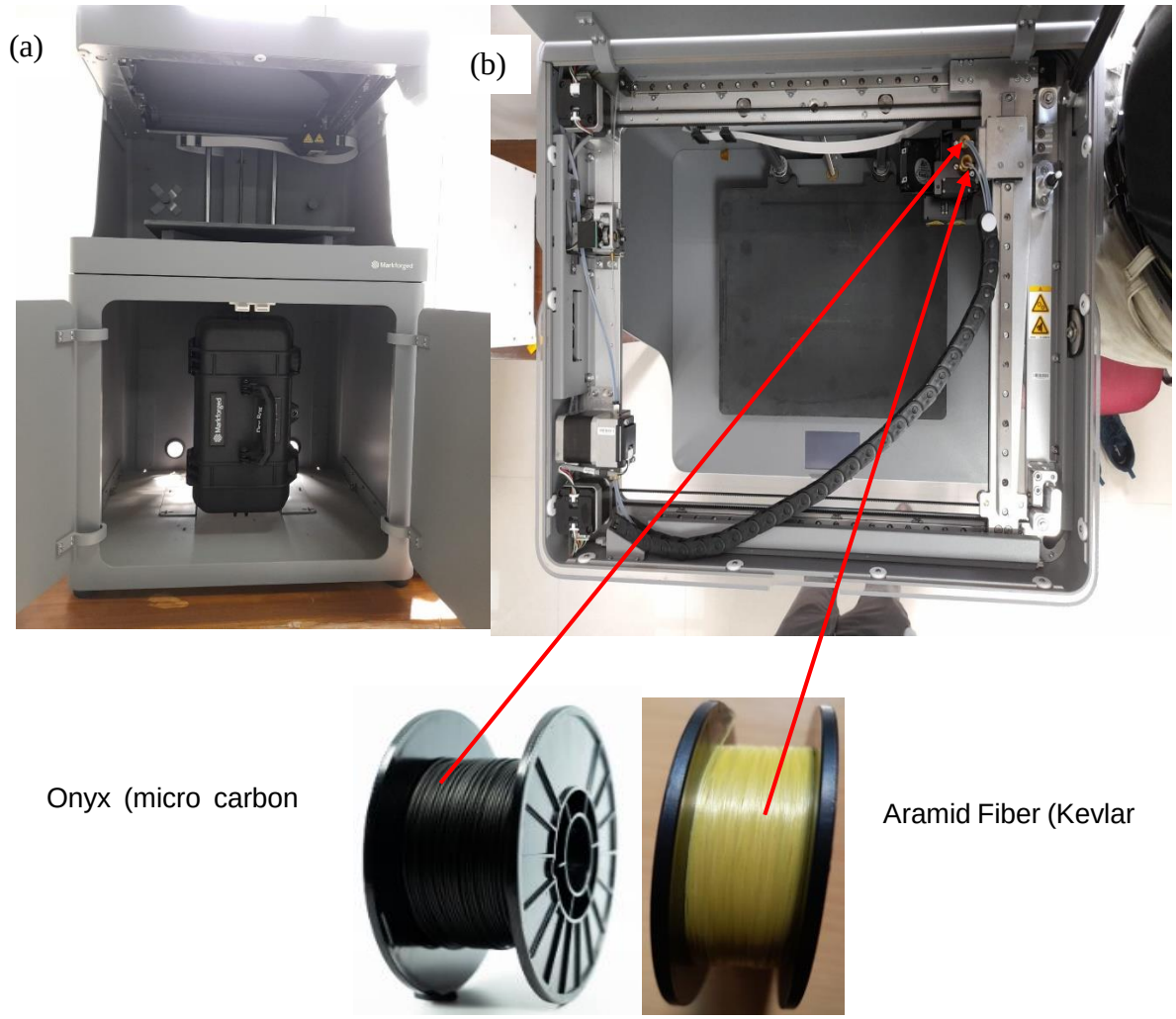

Figure 3.1. (a) General view and (b) detail view of the FDM 3D printer

The setup comprises of a Mark Two commercial 3D printer and its corresponding slicing software called Eiger both supplied by Markforged, Inc. The printer has two extruders, one

for the onyx filament and the other for continuous fibre filament (CFF), and which has a build volume of 330 mm by 270 mm by 200 mm (CFF). The Onyx consists of micro carbon fiber filled nylon produces precise parts with nearly flawless surface finishes. When using CFF, the printer employs a fixed deposition layer with a thickness of 0.125 mm and has the ability to track partially or completely reinforced routes on the addressed region. For the portion that is not reinforced, it also provides four different infill designs.

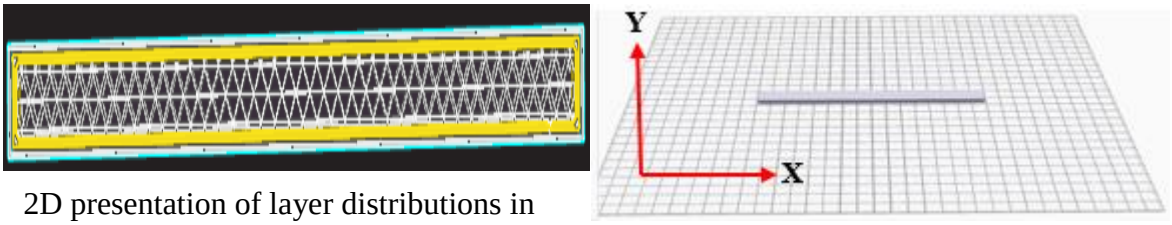

2D presentation of layer distributions in Specimens in the Eiger slicing software

Figure 3.2. Slicing and infill paprameters

Figure 3.2 shows the infill parameters' design and fibre direction. Through the printing nozzle, the filament may be melted into a tape with a width and thickness of around 1 mm and 0.125 mm, respectively. A layer of nylon was created to be on the bottom of specimens in order to make it easier for the CCFRT layers to deposit on the print bed and prevent them from disintegrating while printing [171]. Additionally, a nylon layer was placed to the top for symmetry purposes. The material was chosen from a 1.75 mm diameter Markforged nylon filament that was transparent in black for easy inspection. A Markforged X7 Printer is used to create the specimens, as seen in Figure 3.1 (a). It has an accuracy of 10 m and is an industrial-grade printer. Details are displayed in Figure 3.1 (b). A 0.4 mm diameter nozzle is used to extrude nylon filament during the first stage of the CCFRT printing process, and a 0.9 mm diameter nozzle is used to extrude continuous fibre filament. Print a layer of nylon

floor first, followed by layers of continuous fibre, and then a layer of nylon roofing. Mark-forged Eiger software was used to develop the sample slicing strategy and fibre orientation. It is obvious that the printer offers superb finishing. Unfortunately, this provides the user little control over the orientations and distributions of the fibres, which might reduce the stiffness of the component, particularly for very complicated geometries. Four distinct mechanical tests were carried out in accordance with ASTM norms to fulfil the specific purposes mentioned before. ASTM D 638 technique is used to assess the tensile behavior of composites, ASTM D256 for impact property and ASTM standard D790 for flexural behavior of material. The material was printed using Onyx, and it is reinforced with glass fibre, high-strength, high-temperature fibre, and Kevlar fibre. The deposition layer is 0.125 mm, and the heat nozzle is 270^0C. To verify the authenticity of the results, each test has been carried out three times under the exact identical conditions.

3.3 Tensile tests

This article conducted tensile testing of 3D printed GFRT, HSHTFRT, and KFRT using longitudinal fibre arrangement since the longitudinal mechanical characteristics of composites are often the largest. They designed and produced the standard tensile specimens. It is dumb-bell-shaped specimen according to ASTM D 638 type-I standard. As shown in Figure 3.4, it is concentric filament fill pattern, which is routes fiber back and forth to simulate the separate unidirectional layers of conventional laminates. The thickness of each layer is 0.1 mm with 24 layers. The volume fraction of all 3D printed composite GFRT, HSHTFRT and KFRT is given in Table 3.1. As shown in Figure 3, the tensile tests were carried out using a 100 kN Instron dynamic-UTM machine equipped with an extensometer to measure the lengthening

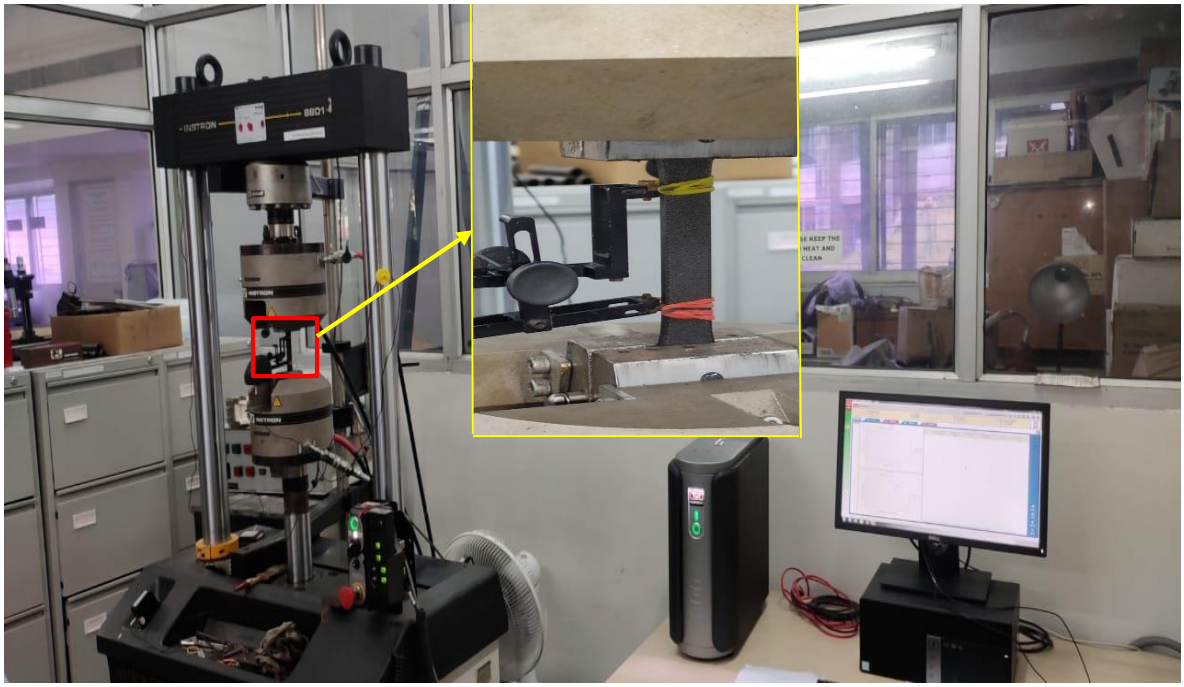

Figure 3.3. Tensile test set-up for investigating the tensile property.

of the material during the first deformation stage. Depending on how long the specimen was, extensometers were chosen. The dumbbell specimens have extensometer gauge lengths that are 50 mm long. The nominal strain may be calculated by dividing the displacement the extensometer recorded by the length of the extensometer gauge. Black and white specks were evenly distributed over the specimen's surface. The specimen was photographed using two cameras. Room temperature and 50% humidity are the test conditions. A 1 mm/min strain rate has been specified.

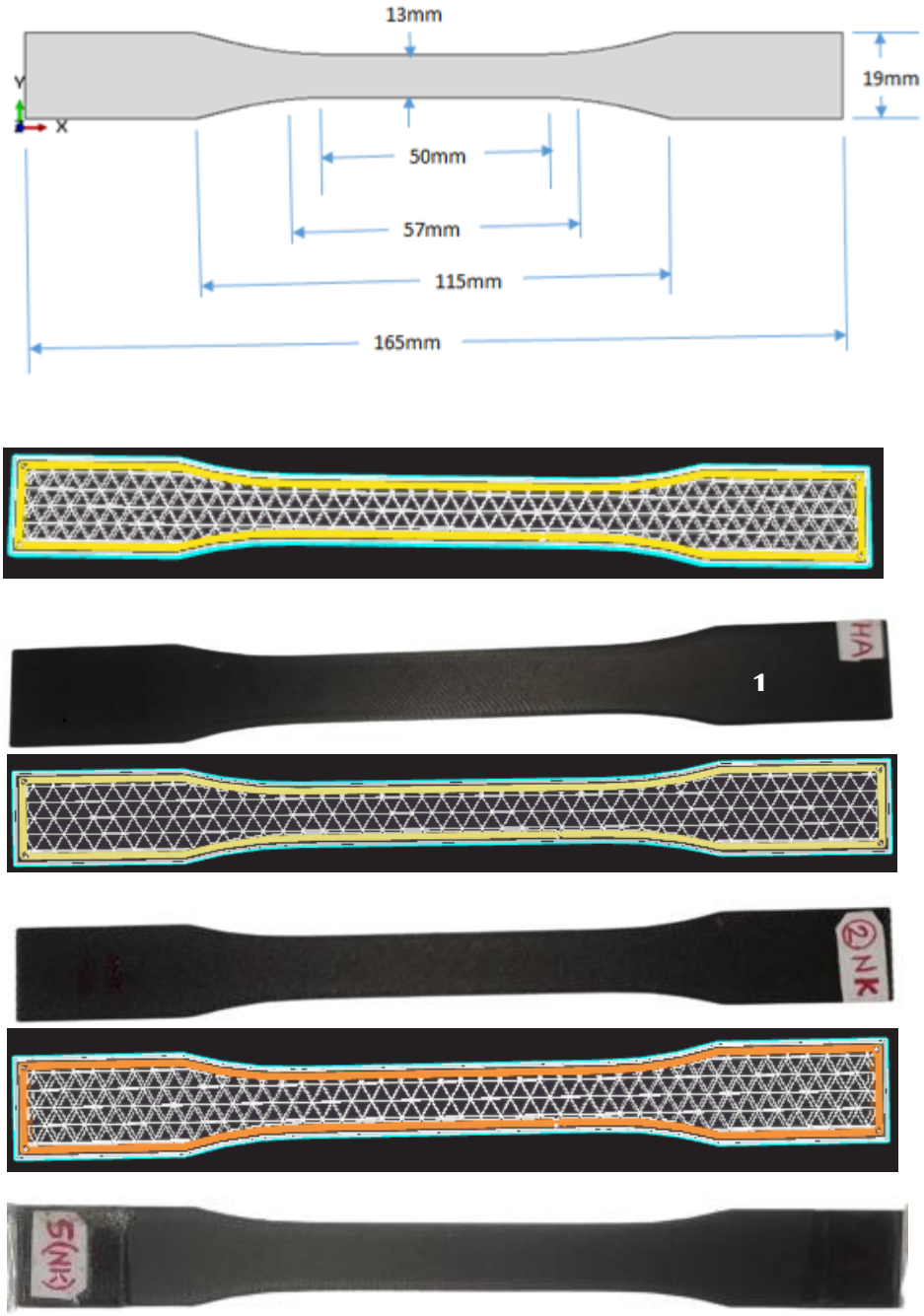

Figure 3.4. Tensile Specimen dimension as per standards ASTM D 638 type-I where 1-KFRT, 2-GFRT and 3-HSHTRT yellow lines represents the fiber filaments and others are matrix (nylon).

Table 3.1. Volume fraction of different 3D printed composite.

Composite types	Theoretical
Glass fiber polymer composite concentric fiber angle zero degree build plate orientation (GFRT)	17.98%
High strength high temperature fiber polymer composite concentric fiber angle zero degree build plate orientation (HSHTFRT)	17.98%
Kevlar fiber polymer composite concentric fiber angle zero degree build plate orientation (KFRT)	17.98%

3.4 Flexural (Three point bending) test

Due to the fact that many materials' physical characteristics, particularly those of thermoplastics, can change with respect to the ambient temperature, testing materials at temperatures that match the environment they are intended to be used in is occasionally necessary.

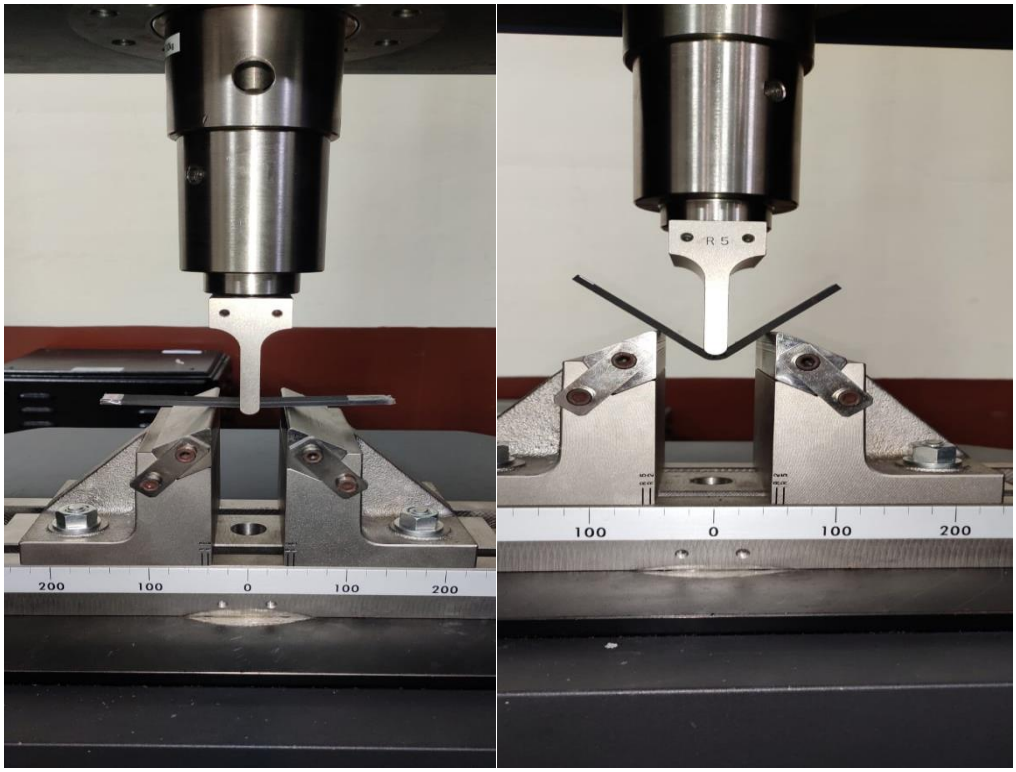

Before test (sample loaded) After test (failed sample)

Figure 3.5. Flexural test set-up.

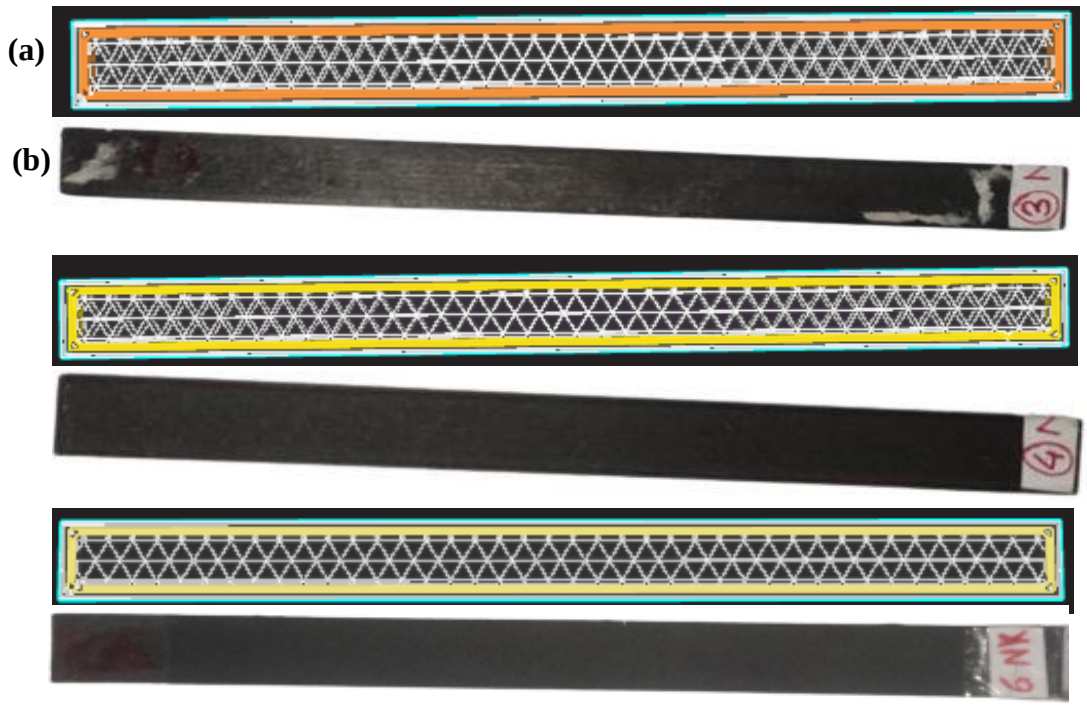

Figure 3.6. Flexural Specimen as per ASTM D 790 where 3-HSHTRT, 4-KFRT 6-GFRT

The flexural test, which is typically applicable to both rigid and semi-rigid materials, resins, and laminated fibre composite materials [56], when a beam is loaded from three points, the force required to bend it is evaluated using composite materials. When selecting materials for sections that won't bend while supporting loads, the information is usually employed. Most commonly, three-point and four-point bend tests in accordance with ASTM D 790 and ASTM D 6272 are used to test the flexural strength of large fiber-reinforced plates and polymer reinforced composites. These tests help to better understand the properties of these materials and make sure they are suitable for the intended application. During the flexural test, the sample is frequently supported by a support span. The loading nose applies the load to the centre, causing three points to bend at a predefined rate. Speed and test mode were both set at 1 mm/min. The three test parameters are the support span, loading speed, and maximum deflection.

Table 3.2. Volume fraction of composite for flexural property

Composite types	Theoretical
Glass fiber polymer composite concentric fiber angle zero degree build plate orientation	29.76%
High strength high temperature fiber polymer composite concentric fiber angle zero degree build plate orientation	29.76%
Kevlar fiber polymer composite concentric fiber angle zero degree build plate orientation	29.76%

These characteristics, which are dependent on the thickness of the test specimen, have a variety of definitions in accordance with ASTM and ISO. In accordance with ASTM D790, the test ends when the sample breaks or exhibits a deflection of more than 5%, but in accordance with ISO 178, the test ends when the sample breaks. If the test is completed without the specimen breaking, the stress at 3.5% (standard deflection) is recorded and the test is continued as far as it can go. Flexural testing offers a semi-qualitative indication of the composite's fiber/matrix interfacial strength [56]. The results of the testing of flexural properties involve customizable and raw data on the flexural strength at yield point, the strain, the flexural strength at breaking point, the flexural strength at 5.0% (ASTM) deflection, the modulus of elasticity, and the stress/strain curves. How stiff a material is measured by its flexural modulus. As depicted in Figure 3.6, the bending specimens were created in accordance with ASTM D790 [57] standard. The actual measurements are 125 mm × 12.7 mm × 4 mm. Figure 3.6 depicts the three types of reinforcements that were taken into consideration. The volume fraction of composite is 29.76% and it is given in Table 3.2. On the testing apparatus depicted

in Figure 3.5 the three-point bend technique was used to evaluate the flexural parameters such as flexural strength and flexural modulus.

3.5 Impact tests

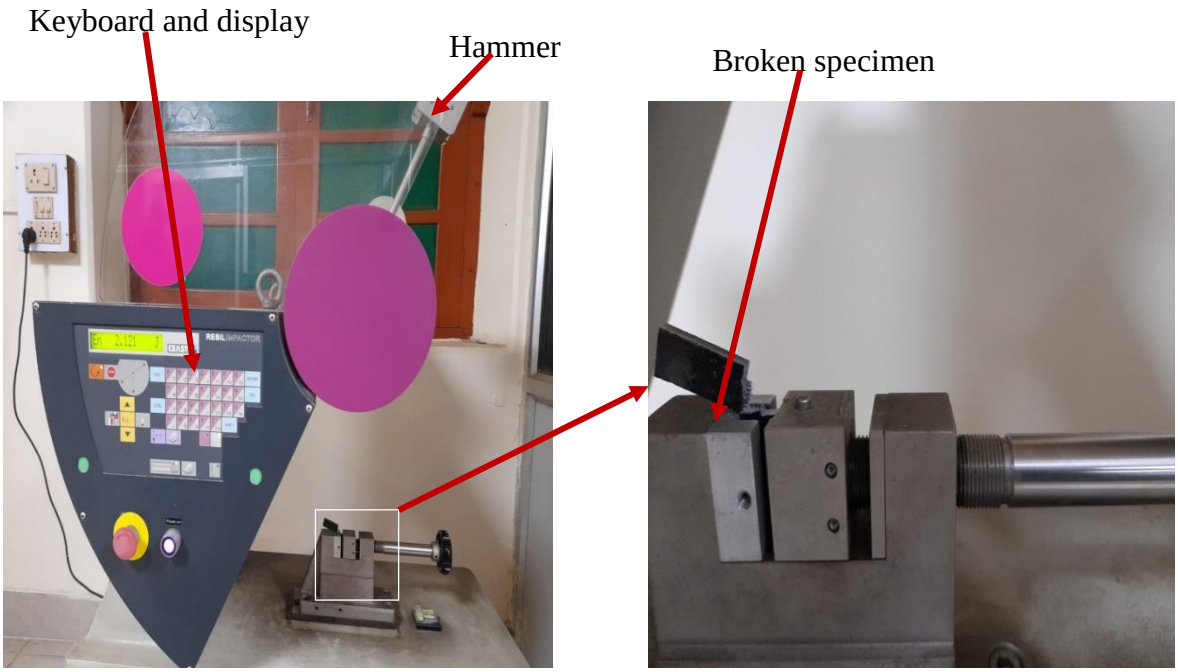

Figure 3.7. Resil impact test set-up for investigating the impact behavior of composites.

The objective of the impact test is to determine how a specimen of a known material, such as polymer based composites, would respond to a sudden spike in stress. Engineering materi als tensile strength, brittleness, notch sensitivity, and impact resistance to withstand high-rate loading are specifically assessed using the impact test [59]. In terms of product liability and safety, the ability to measure the impact property is quite advantageous. Types of impact test specimens include V-notch configurations with three different reinforcements (glass fiber, high strength high temperature glass fiber and Kevlar fiber) and two different build plate orientations (0^0 and 90^0). Here Izod specimen configuration are used for calculation of impact property.

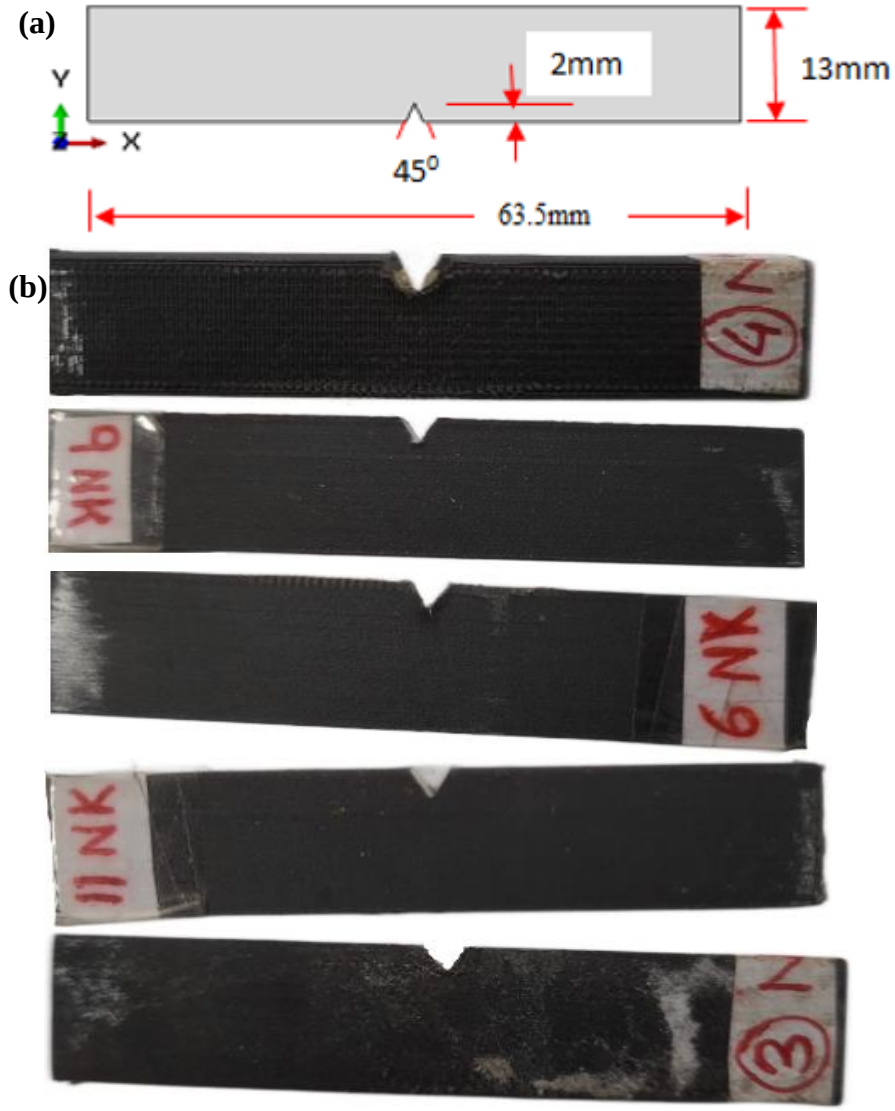

Figure 3.8. Impact Specimen as per ASTM D 256 where 3-HSHTRT(0^0), 4-KFRT (0^0) 6-GFRT (0^0), 9-HSHTRT (90^0) and 11-KFRT (90^0)

In the Izod impact test, the notch is directed towards the striker. For evaluating the impact performance of FRP composites produced via 3D printing, there are no established test procedures. As shown in Figure 3.8, the impact specimens for this study were created in accordance with the ASTM D 256 standard. The key measurements are displayed in Figure 3.8 (a). Figure 3.8 (b) shows the original specimen with a U-shaped notch. The printed specimen is machined to create the notch. Figure 3.6 (a) displays three different internal fibre layout

types. The volume fraction of different 3D printed composite is shown in Table 3.2. Impact testing tools were selected according to ASTM standard D256 to ascertain the impact strength of the fibre. Five samples of each kind were evaluated in order to lower measurement discrepancies related to energy dissipation. The CEAST resil impactor of energy 5.5 J with a tester in the pendulum type was used to conduct the impact test (Figure 3.7). It is specifically made for testing impacts with energies ranging from 1 to 25 J. The difference between the impactor's initial and final heights represents the energy lost during specimen fracture. The specimen fractured as a result of the force of the pendulum coming down from a 1350-foot height. During the experiment, the composite's energy absorption was measured and examined. With the use of the following equation (3.1), the total amount of energy needed to break the specimen is calculated

$$E_T = mg(h_0 - h_f) \pm 0.2J \qquad (3.1)$$

Where $E_{.T.}$ =Total energy; g = acceleration due to gravity; m = mass; h_0 = initial height and h_f = final height.

The impact strength or resilience is defined as total absorbed energy per unit cross-sectional area (kJ/m^2) following the ASTM standard D256

$$E_C = \frac{E_T}{wt} \qquad (3.2)$$

Where t = thickness and w = width of specimen. The energy losses owing to air resistance have been taken into account. However, other losses due to bearing friction are neglected due to their small magnitude.

3.6 Machining

3.6.1 Experimental Set-up

The three-axis Micro CNC milling machine set-up was used for slot cutting operation having dimension Length = 15mm; diameter of cutting tool = 2.5mm; depth of cut = 1.05mm. The different components of the machining set-up are shown in Figure 3.9. The maximum travel of the work table is 145, 50 and 50mm in X, Y, and Z directions, respectively. This machine has a position accuracy of $\pm 5\mu m$ for the entire range and with all three axes and has $\pm 1\mu m$ repeatability for all three axes. For all three axes, the slide is $\pm 1\mu m$ straight. The machine's spindle is driven by a D.C. motor with a speed range of 1220–3461 rpm. All the experiments have been performed on the three axes micro CNC milling machine. This machine consists of four motors, where three motors are used for three axes movement and the 4^{th} one for controlling the speed of the cutting tool. There are a total of ten different speed variations available from 1220 rpm to 4461 rpm. The input parameters are rpm, feed, and material, which were varied, relating one parameter to another to obtain the best output. Input parameters that changed throughout the machining process were Tool speed (rpm), feed (rev/min) and material. Secure the three types of 3D printed composite sample such as HSHTRT(0^0), 4-KFRT (0^0) and GFRT (0^0) into the holder by tightening the screws of the workpiece holder. The titanium-coated ultra-fine grain cemented carbide rod of 2.5 mm in diameter was used as a cutting tool. The cutting tool was mounted to the spindle, and an N.C.

command was used to rotate the spindle.

3.6.2 Experimental Design

The optimal design parameters were determined using the Taguchi L_9 orthogonal array for improved performance and cost [61]. Based on the study reported in the domain of non-conductive materials, the input parameters and their values were chosen [62]. Each experiment set was repeated at least three times to eliminate any random fluctuation in the experimental results. This method can drastically minimise the number of experiments required, which is essential to get the necessary data. In this investigation, the experimental plan has cutting speed (rpm), feed and different materials as the governable variable. Based on previous non-conductive material, the various input parameters and levels were identified [63]. Each trial was performed three times to remove any random fluctuations in the experimental results. Table 3.3 contains a list of the machining input parameters and their levels that were taken into account throughout the experiment. The outcomes from the experiments were done by applying Taguchi's L_9 orthogonal array as shown in Figure 3.19. Our primary target is to increase the MRR, which results in higher productivity, so the S/N ratio can be calculated as "larger the better". The intrinsic influence of input parameters on the MRR is shown in Figure 3.19. Table 3.7 depicts the L_9 orthogonal array used in the investigation. The "larger the better" option has opted for the response (MRR). S/N ratios are computed theoretically using equation (3.3). Optimization techniques on the basis of Taguchi method were performed using minitab

$$\frac{S}{N} = -10log\left[\frac{1}{n}\sum_{i=1}^{n} y_i^2\right] \quad (3.3)$$

Where,

y_i = observed data obtained from experiments and n = number of experiments

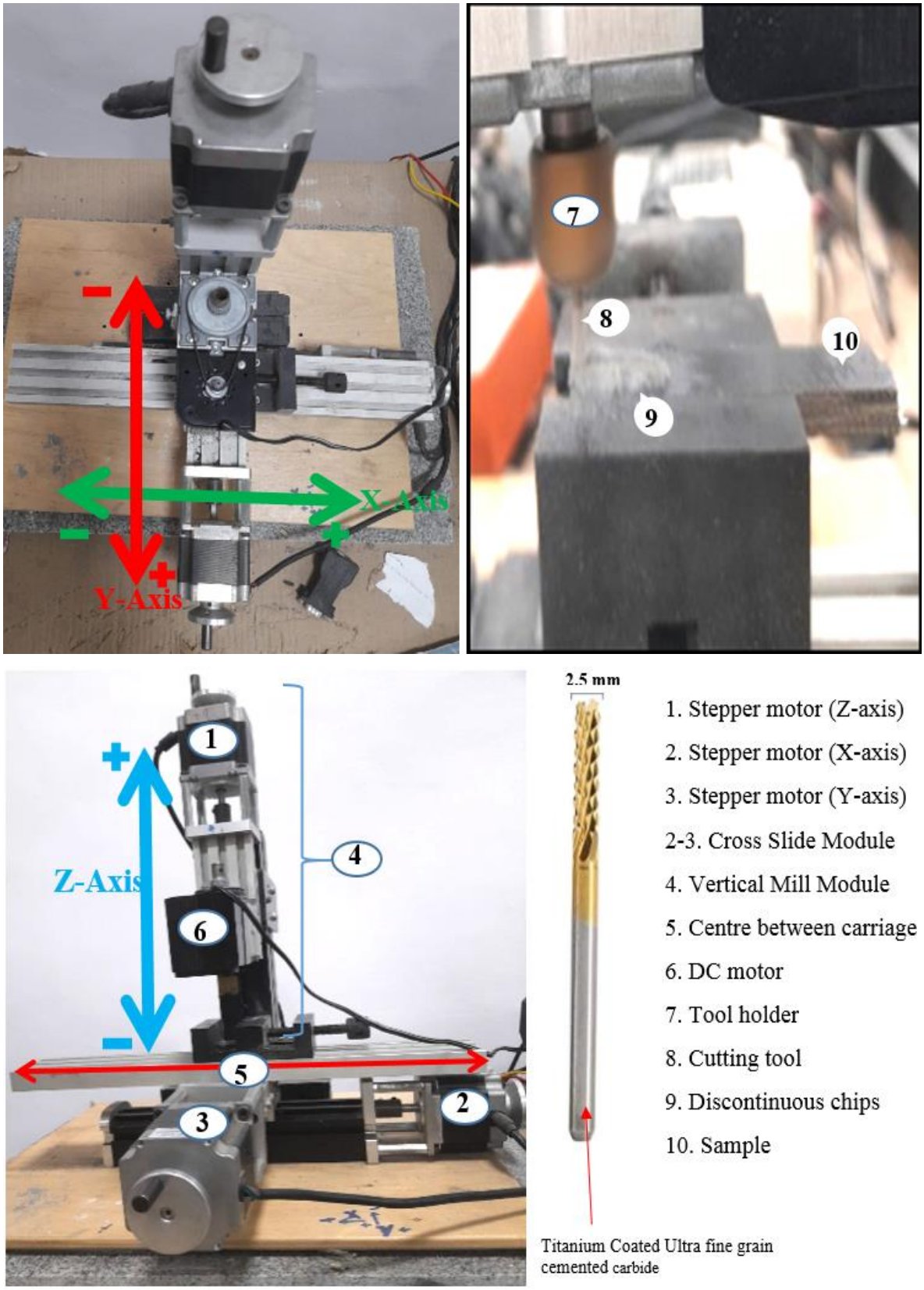

Figure 3.9. 3-axis micro CNC milling machine set-up

Table 3.3. Process parameters with different operating levels.

Input parameter	Level 1	Level 2	Level 3
Tool speed(rpm)	1220	1335	1490
Feed	10	20	30

3.7 Density and specific gravity of composites by displacement method

Density, which would be evaluated in accordance with ASTM D1895 standards and is described as the mass of the material per unit volume, is one of the most important factors in determining the properties of polymer fiber reinforced composite materials [65]. Its value in fiber-reinforced polymer composites mostly depends on the ratio of matrix to reinforcement. When measuring a sample in air and then again while hung on a wire and submerged in water, the difference in weight in the water is observed to calculate the density of the composite constituents (fibres and matrices). When the specimen's density is less than that of water, a sinker may be attached with a wire to make immersion easier. Equation (3.4) is then used to compute the density.

$$\rho = \frac{(0.9975)a}{(a + w - b)} \qquad (3.4)$$

Where a represents the weight of the specimen in the air, b represents the combined weight of the specimen and sinker when fully submerged, and the weight of the wire while partially submerged is represented by w. Similar principles are used to determine a composite's density. In some circumstances, the ASTM D1895 standard is used to assess composite density, by applying equation *(3.5)* where m denotes the composites' mass and v denotes their volume.

$$Density\ (g/cm^3) = \frac{m}{v} \qquad (3.5)$$

Table 3.4. The calculated density of different 3D printed composites.

Serial no	Composite Type	Density (g/cm^3)
1	GFRT (0^0)	1.2691
2	HSHTRT(0^0)	1.2412
3	KFRT (0^0)	1.1214

3.8 Thermal Stability of Polymer Nanocomposites

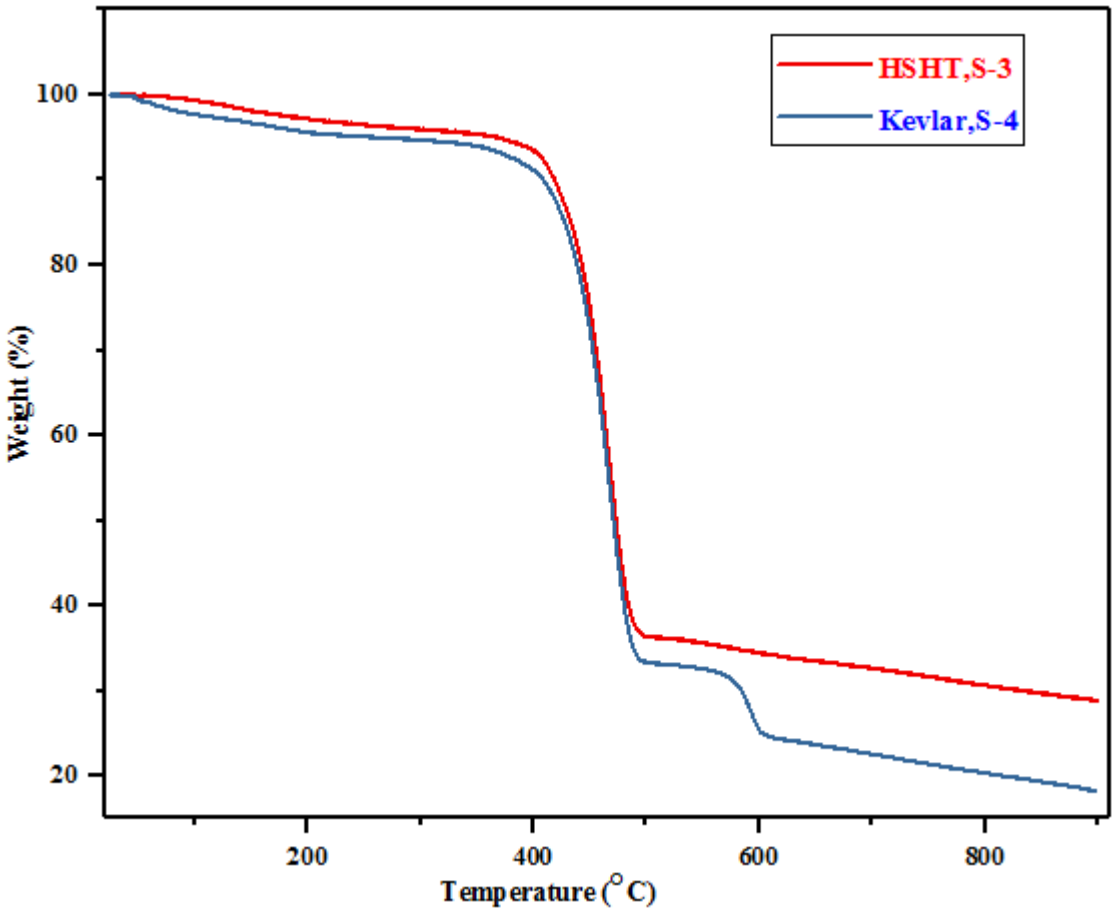

Figure 3.10. TGA curves of HSHTFRT (0^0) versus KFRT (0^0).

The performance of polymer materials during combustion is highly correlated with their thermal degradation characteristics. The thermal degradation behaviour of polymer materials

has been extensively studied using TGA [66–68]. The thermal gradient analysis (TGA) method was used to assess 3D printed composite thermal stability and degradation characteristics and also the adsorption quality. Thermal degradation occurs in one stage for HSHT-FRT (0^0) composite having 29% material and 19% KFRT (0^0) composite material still at 900°C, respectively. In comparison to KFRT (0^0), both HSHTFRT (0^0) composite and GFRT (0^0) exhibit similar degradative behaviour.

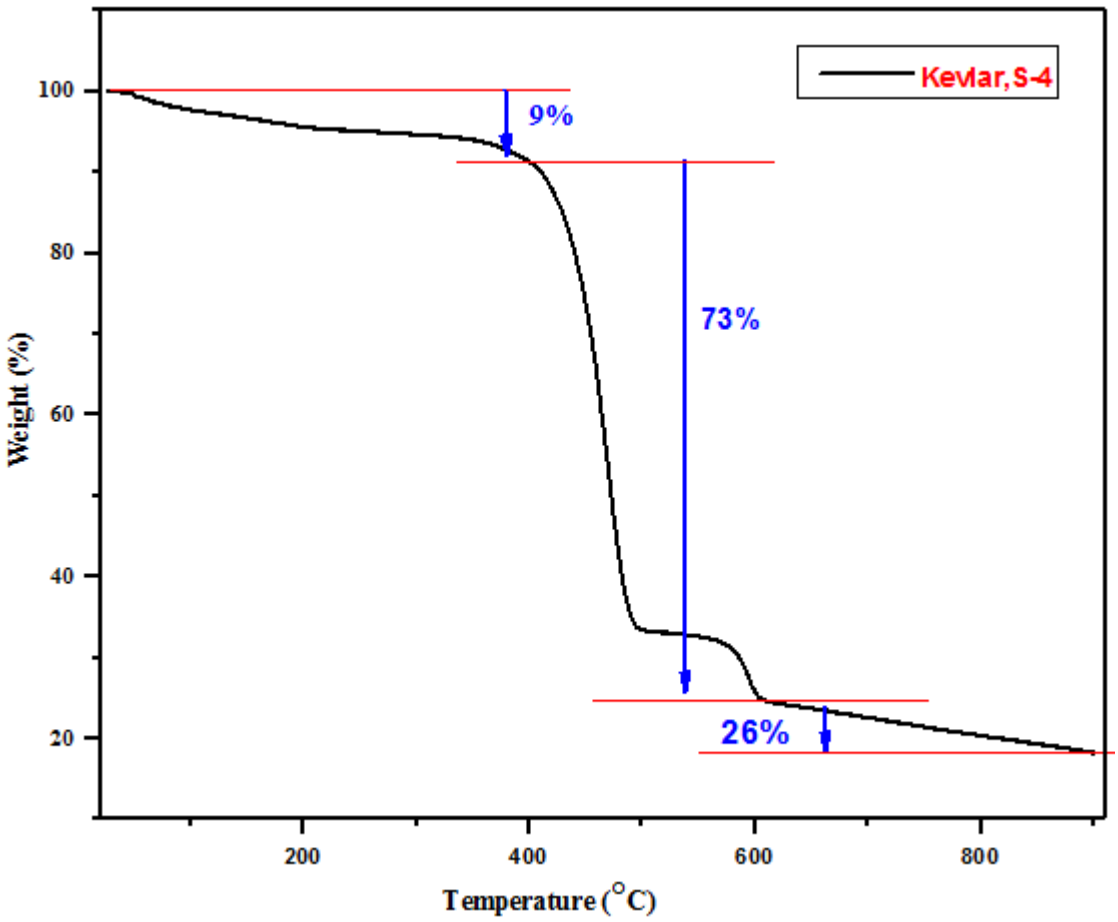

Figure 3.11. TGA curves of KFRT (0^0).

Table 3.5. Calculation of specific surface area for the use of this materials as an adsorbent

Serial number	Composite	Specific surface area (m^2/g)
1	HSHTFRT (0^0)	2489
2	KFRT (0^0)	2931
3	GFRT (0^0)	2561

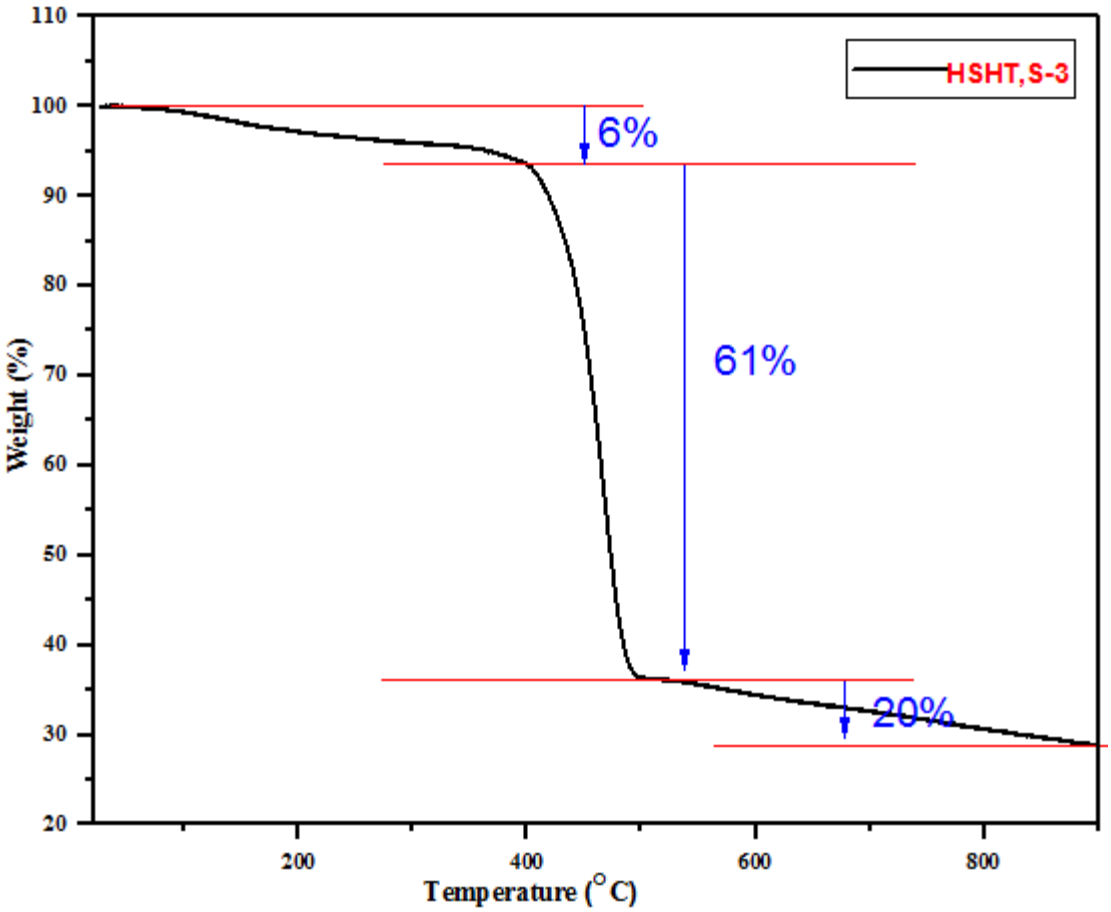

Figure 3.12. TGA curves of HSHTFRT (0^0).

However, HSHTFRT (0^0) composite samples shows excellent thermal stability, as evidenced by the weight (%) loss of 6 % for HSHTFRT (0^0) composite and 9 % for KFRT (0^0) from 0^0C to 400^0C. The increased residue of 29% HSHTFRT (0^0) composite and 19% KFRT (0^0) composite material at 900°C provides additional evidence of better thermal stability. The

specific surface area is calculated from the TGA plot, and it is found that KFRT (0^0) composite material has the maximum area, which is the evidence of highly adsorbent material compared with the other two materials HSHTFRT (0^0) and GFRT (0^0) from Table 3.5.

3.9 Results and discussion

Tensile, flexural, impact, and machining characteristics are used to examine the influence of different reinforcements such as glass fiber, high strength high temperature glass fiber and Kevlar fiber on the mechanical behavior of 3D printed composites.

3.9.1 Stress–strain curves

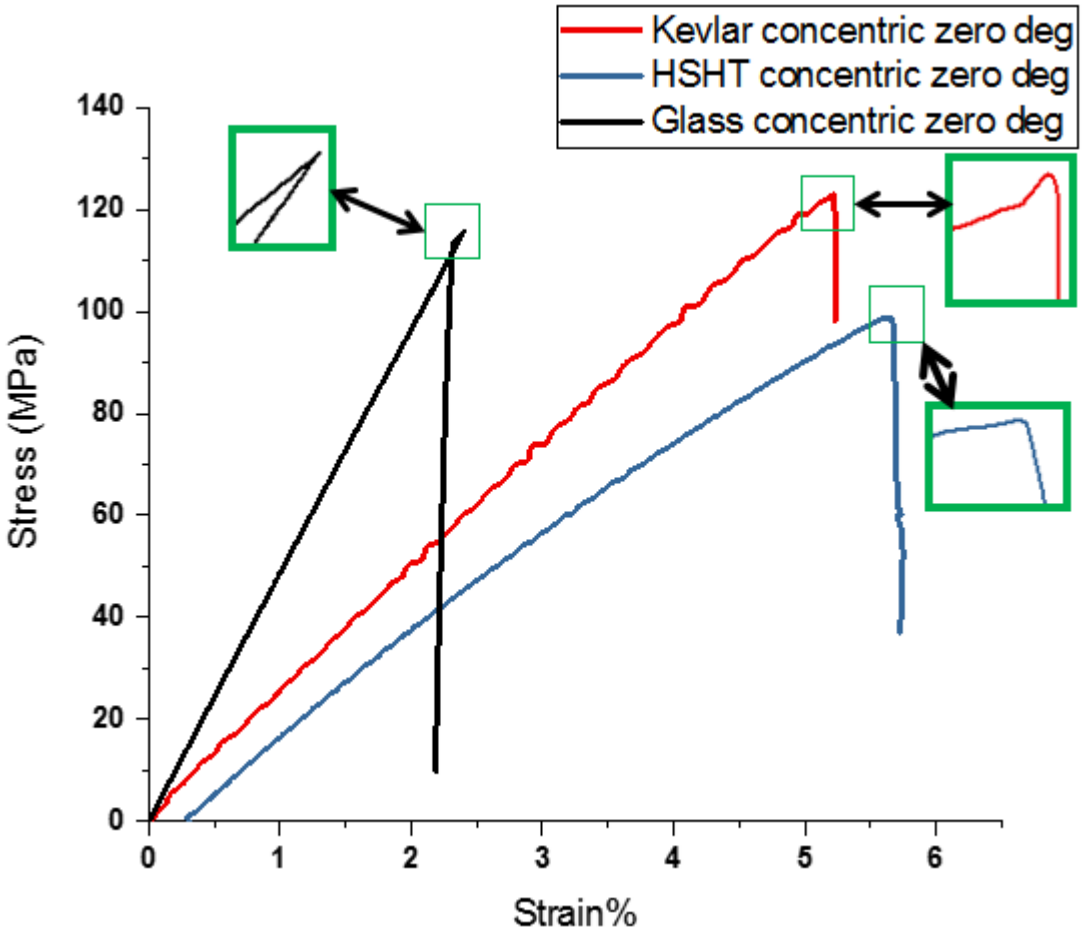

Figure 3.13. Stress–strain plot describing of a tensile behavior of 3D printed composite.

Table 3.6. Tensile properties of 3D printed composite.

Properties	ASTM standard	Concentric Zero degree		
		Glass fiber	Kevlar fiber	HSHT fiber
Max. elongation (mm)	ASTM D638	2.4	5.2	5.7
Peak load (N)	ASTM D638	116	5002	7407
Stiffness (N/mm)	ASTM D638	3556	2280	2726

In this investigation, the tests of dumbbell quasi-static tension, specimens were carried out. It is evident that reasonable levels of experimental reproducibility are achieved. Table *3.6* provides a summary of the comprehensive tensile mechanical characteristics. Tensile strength and % elongation are used to investigate this phenomenon. Figure 3.13 depicts the stress-strain curves, which indicate how different fibre polymer composite specimens of varying concentric fibre rings and fibre layers, combined with the Nylon filled structure. Initially, the load may be supported by the area of contact between the test fixtures and the specimens. Because of this, it shows less slope and curve strength at that time and doesn't fully grasp until after [73,75]. The 3D printed polymer composite sample eventually hits the yield point and breaks. Figure 3.13 shows that for all three types of fibre printed composites, stress and strain both rise as concentric fibre rings and fibre layers increase, which is similarly documented and consistent with other findings [76,77]. Although the Nylon matrix did not break, the fibres did within the specimen. Because nylon is a polymer, it is more elastic. However, when the number of concentric fibre rings and layers increases, the specimen breaks abruptly and clearly exhibits brittleness. The results for elastic modulus and tensile strength that were determined through experimentation are shown in Table 3.6, together with several designable complicated filled Nylon structures on various continuous fibre printed

polymer composite specimens.

3.9.2 Tensile strength

Examining the tensile strength of continuous fibre printed polymer composite sample. The mean tensile strength for the three different sample configurations of continuous fibre printed polymer composites is shown in Figure 3.13. As previously stated [79], it was found that The inclusion of concentric fibre rings and fibre layers further improves the tensile strength of the 3D-printed polymer composite specimen. The continuous kevlar fiber reinforced thermo-plastic (CKFRT) composite showing the maximum tensile strength of 124 MPa followed by glass FRT (CGFRT) having tensile strength of 116 MPa and High Strength High Tempera ture Fiberglass FRT (CHSHTGFFRT) composite showing the least value of tensile strength of 99 MPa similar type of explanations is also reported elsewhere [72]; it is due to the differ-ence in strength of individual fiber where the kevlar having the strength of 610 Mpa followed by HSHT FG of 600 MPa fiber glass is having the least value of 590 MPa [70] but here the important point is that the difference in strength is only 10 MPa between each succeeding fiber while these difference are larger in case of final fabricated composites. The tensile strength of continuous GFRT is 116 MPa which is greater than the value found in ref. [71]. The order of tensile strength is as follows: Kevlar fiber reinforced thermoplastic 3D printed polymer composites (KFRTC) > glass fiber reinforced thermoplastic 3D printed polymer composites (GFRTC) > High strength high temperature glass fiber reinforced thermoplastic 3D printed polymer composites (HSHTGFRTC).

3.9.3 Ductility

The longitudinal tensile failure strain of High strength high temperature glass fiber reinforced thermoplastic 3D printed polymer composites (C-HSHT-GF-FRT) is approximately 5.65%

and it is the highest value of failure strain compared with other two composites. The amount of percentage elongation is the indication of ductile nature of material hence C-HSHT-FRT composite is preferred where ductile nature is needed. The longitudinal tensile failure strain of Kevlar fiber reinforced thermoplastic 3D printed polymer composites (KFRTC) is 5.22%. The longitudinal tensile failure strain of glass fiber reinforced thermoplastic 3D printed polymer composites (GFRTC) is 2.4%. Therefore from the stress-strain curve it is found that the most brttle behavior shown by glass fiber reinforced thermoplastic 3D printed polymer composites (GFRTC). Moreover, the nature of the curve is also the confirmation of brittle behavior of material. The glass fiber reinforced thermoplastic 3D printed polymer composites (GFRTC) have the sharp yield point compared with other two composites as it is easily visible in enlarged view. The order of sharpness in the yield point is as follows: Glass fiber reinforced thermoplastic 3D printed polymer composites (GFRTC) > Kevlar fiber reinforced thermoplastic 3D printed polymer composites (KFRTC) > High strength high temperature glass fiber reinforced thermoplastic 3D printed polymer composites (HSHTGFRTC).

3.9.4 Elastic modulus

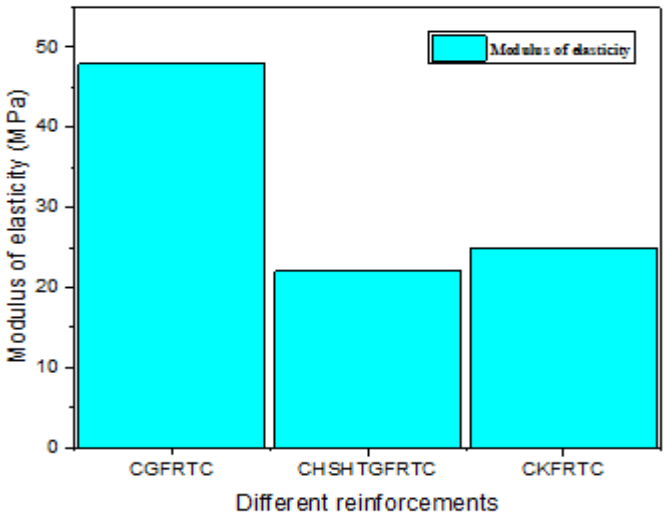

Figure 3.14. Elastic modulus of 3D printed composites.

The stress-strain curves for each sample were used to determine its elastic modulus, as shown in Figure 3.13. Modulus of elasticity is a measure of stiffness. Figure 3.14 displays the mean elastic modulus of three distinct continuous fibre printed polymer composite samples, which demonstrates that the composite having highest value of failure strain having least value of young's modulus and as the ductility of material decreases the value of stiffness increases [80,81]. Elastic modulus is listed in the following sequence: Glass fiber reinforced thermoplastic 3D printed polymer composites (GFRTC) > Kevlar fiber reinforced thermoplastic 3D printed polymer composites (KFRTC) > High strength high temperature glass fiber reinforced thermoplastic 3D printed polymer composites (C-HSHT-GF-FRT).

3.9.5 Three point bending properties

Figure 3.15 represents the bending force-displacement curves and their failure mechanisms of three different 3D printed composites Glass fiber reinforced thermoplastic (GFRTC), Kevlar fiber reinforced thermoplastic (KFRTC), High strength high temperature glass fiber rein forced thermoplastic (HSHTGFRTC). There are clear differences present. The ASTM D790 standard defines the flexural modulus E_b as

$$E_b = \frac{L^3 m}{4bh^3} \tag{3.6}$$

where L denotes the span's length, b denotes its width, h denotes its thickness, and m denotes the slope of the load-displacement curve's linear part.

The flexural strength is defined as

$$\sigma_b = \frac{3F_{max}L}{2bh^2} \tag{3.7}$$

where, F_{max} is the maximum flexural force.

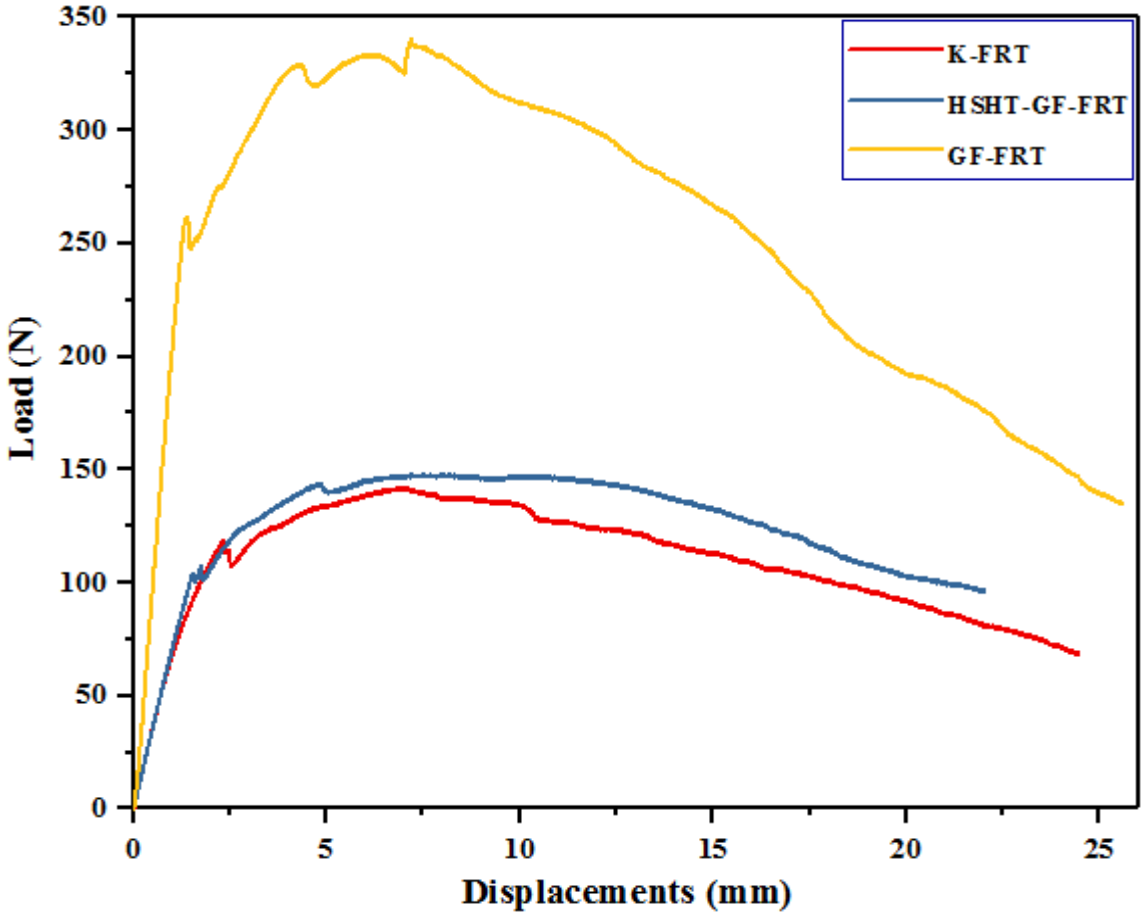

Figure 3.15. Force-displacement curves and their failure mechanisms of bending specimens

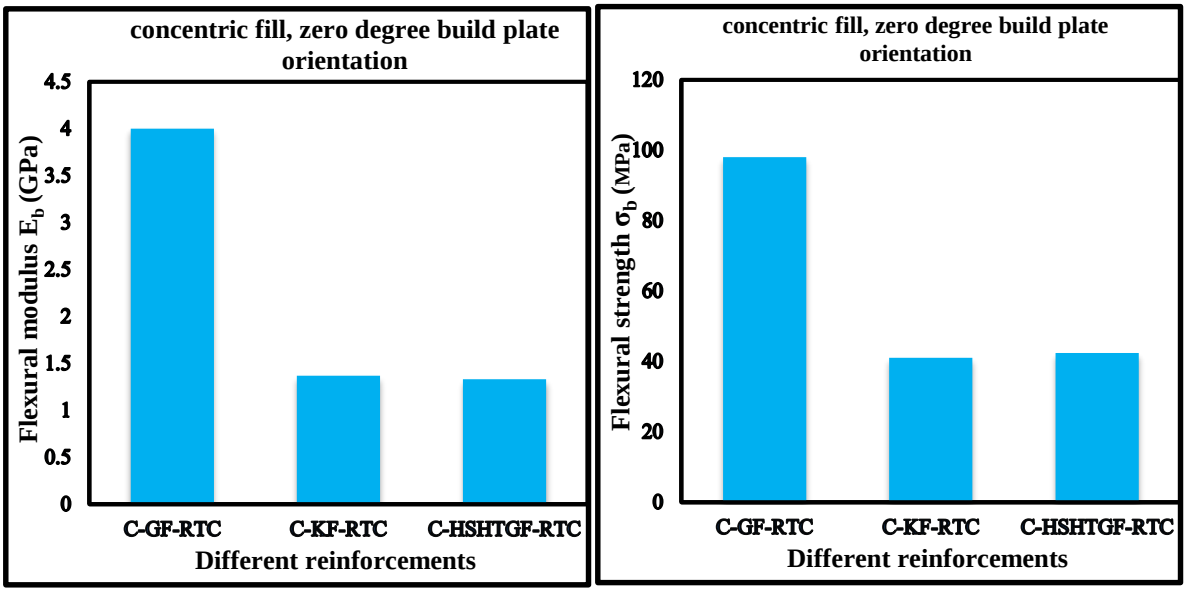

Figure 3.16. Effect of different reinforcements on flexural properties.

The flexural properties are shown in Figure 3.16. The flexural strength and modulus of continuous glass fiber reinforced thermoplastic are 98 MPa and 4 GPa, respectively. Under bending strain, the specimen's fracture surface can be divided into upper compressive and lower tensile areas. Compression failure in the fibres and matrix fracture are the failure mechanisms in the upper area. Fiber tensile failure, fibre pull-out, and matrix fracture are, by contrast, those of lower region. The two primary failure mechanisms for the longitudinal layers under compressive load are matrix fracture and fibre compression failure. The major failure mechanisms for the longitudinal layers under tensile stress are fibre tensile failure, fibre pull-out, and matrix fracture. The principal failure mechanisms for the transverse layers are matrix fracture, fiber/matrix debonding, and fibre shear failure. The matrix's evident river-like structure denotes brittle fracture. Additionally, the longitudinal and transverse layers failed due to delamination. The order of bending properties is as follows: Glass fiber reinforced thermoplastic 3D printed polymer composites (GFRTC) > Kevlar fiber reinforced thermoplastic 3D printed polymer composites (KFRTC) > High strength high temperature glass fiber reinforced thermoplastic 3D printed polymer composites (HSHTGFRTC).

3.9.6 Impact properties

3.9.6.1 Energy absorption capacity

The calculated results, as shown in Figure 3.17 reveal that continuous Kevlar fiber reinforced thermoplastic (KFRT) has the least energy absorption capacity, C-HSHT-FRT has 69% more and Glass fiber RT has the highest energy absorption capacity of 76% more in the case of V-notch because composites have stiff and rigid fibres. However it can be seen that there is a huge impact on build plate orientation. The ninty degree specimen having 71% more energy absorption capacity compared with zero degree specimen in case of Kevlar FRT. But in case

of HSHT-FRT composite there is only 6% improvement in energy absorption capacity.

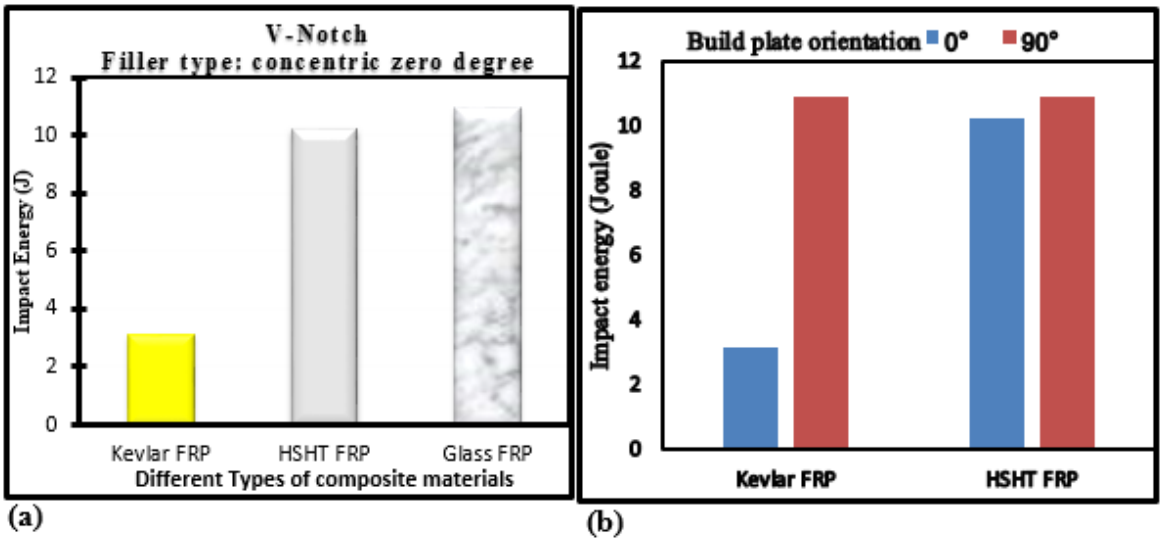

Figure 3.17. Energy absorption charts showing (a) the effect of different reinforcement (b) the effect of build plate orientation

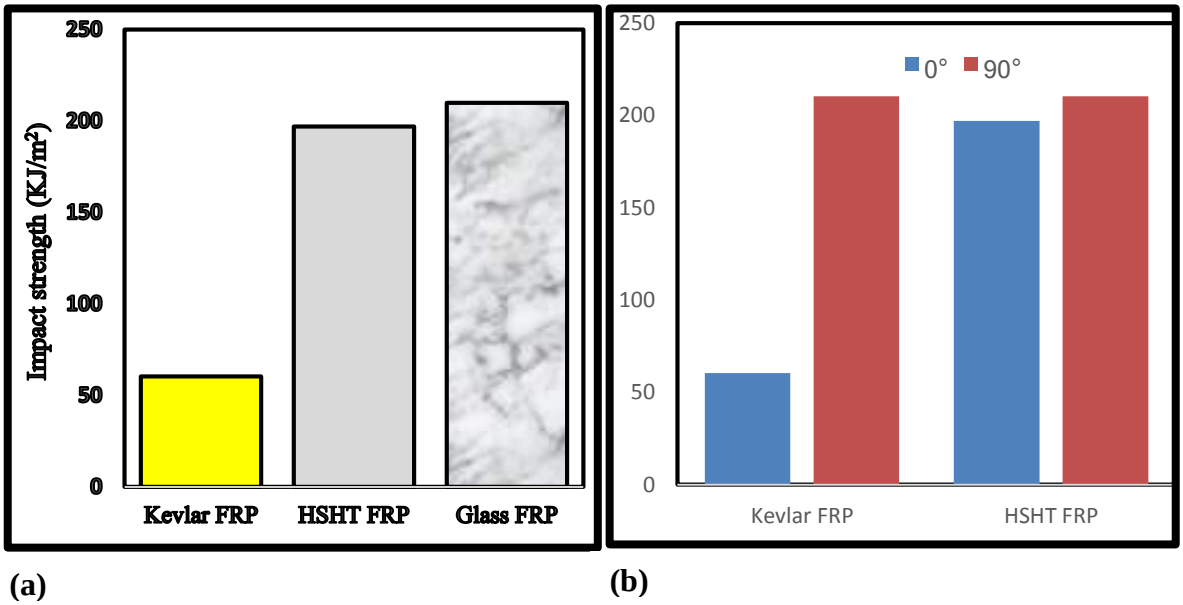

Figure 3.18. Comparison of impact strength of (a) different 3d printed composite and (b) build plate orientation

3.9.6.2 Impact strength

The effect of different reinforcements on impact strength is shown in Figure 3.18(a). The order of bending properties is as follows: Kevlar fiber reinforced thermoplastic 3D printed polymer composites (KFRTC) > High strength high temperature glass fiber reinforced thermoplastic 3D printed polymer composites (HSHTGFRTC) > Glass fiber reinforced thermoplastic 3D printed polymer composites (GFRTC). The effect of build plate orientation on impact strength is shown in Figure 3.18(b). The KFRT composite experiences huge impact of plate orientation compared with HSHT-FRT composite.

3.9.7 Taguchi Analysis and ANOVA

The outcomes from the experiments were done by applying Taguchi's L_9 orthogonal array as shown in Table 3.7.

Table 3.7. Experimental results for MRR

Expt. no.	Tool speed (rpm)	Feed (mm/rev)	MRR (mg/min)	S/N ratio (db)
1	1220	10	1.8769	5.4688
2	1220	20	1.9549	5.8225
3	1220	30	4.6749	13.3954
4	1335	10	1.9569	5.8314
5	1335	20	5.4836	14.7813
6	1335	30	6.0184	15.5896
7	1490	10	3.7169	11.4036
8	1490	20	5.3730	14.6043
9	1490	30	6.9120	16.7921

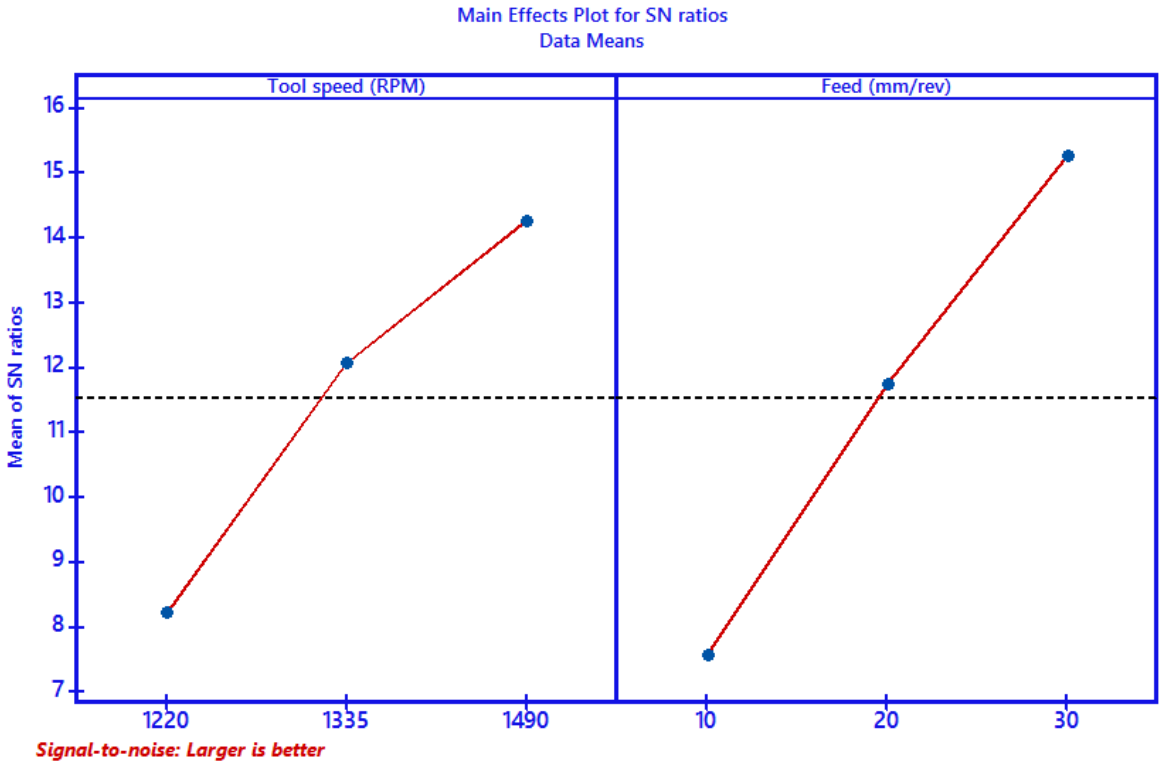

Figure 3.19. Main effect plot for S/N ratios for MRR

Table 3.8. Response Table for Signal to Noise Ratios (Larger is better)

Level	Tool speed (RPM)	Feed (mm/rev)
1	8.229	7.568
2	12.067	11.736
3	14.267	15.259
Delta	6.038	7.691
Rank	2	1

Our primary target is to increase the MRR, which results in higher productivity, so the S/N ratio can be calculated as "larger the better". The intrinsic influence of input parameters on the MRR is shown in Figure 3.19. The relative slope of the linear graph indicates the importance of input parameters. The slope of the graph depicting the influence of feed rate on MRR is clearly higher than that of the other two graphs, as shown in the figure. Hence it can be concluded that the feed rate heavily influences the MRR; tool speed is relatively important,

while the material is the least important factor. It can also be deduced from the graph that the MRR increases as the feed rate increases, owing to the fact that as the feed rate increases, the cutting force increases as well. MRR reduces as tool spindle speed increases. The cutting force lowers as the tool spindle speed increases because the coefficient of friction decreases as rotational speed increases. This effect is higher at a lower speed, and as the speed increases, this effect is going to decrease. In order to determine the impact of a factor on machining performance, the ANOVA test was used with a 95% confidence level [82]. The Fisher test (F-value) has been used to examine the maximum machining parameter values that indicate the most important influencing elements on the process performance. Alternatively, the P-value shows whether a process parameter is significant or not; if the P-value is less than 0.05, then the factor is significant. Table 3.9 shows the analysis of variance for material removal rate. It can be shown that the feed has the maximum percentage contribution to the variance revealed by MRR, followed by tool speed and then material.

Table 3.9. Analysis of variance for Material removal rate

Source	DF	Seq SS	Contribution	Adj SS	Adj MS	F-Value	P-Value
Tool speed (RPM)	2	9.685	32.71%	9.685	4.8427	6.32	0.058
Feed (mm/rev)	2	16.861	56.95%	16.861	8.4306	11.01	0.024
Error	4	3.063	10.34%	3.063	0.7657		
Total	8	29.610	100.00%				

The low error percentage of 12.69 demonstrates the model's fitness [83]. Table 3.8 displays the responses for S/N ratios for MRR. The level that shows the highest S/N ratio for each input parameter is the optimum level. Table 3.8, shows that Level 1 for feed, Level 2 for tool speed, and Level 3 for material are the optimum levels for the highest MRR. The outcomes

from the experiments were done by applying Taguchi's L_9 orthogonal array where the design matrix shows that Exp. No. 9 represents the ideal set of input parameters for MRR as shown in Table 3.7. Our primary target is to increase the MRR, which results in higher productivity, so the S/N ratio can be calculated as "larger the better". The intrinsic influence of input parameters on the MRR is shown in Figure 3.19. Table 3.7 depicts the L_9 orthogonal array used in the investigation. The "larger the better" option has opted for the response (MRR). Since the trials were already carried out three times with the ideal input values, there is no need to conduct confirmation experiments. The suitability of the model is determined to be adequate for further research. The conclusion from the analysis of variance in this study might be sent for additional analysis to forecast. Table 3.10 includes the values of the input parameters at their optimum levels. According to regression analysis, equation (3.8) provides the regression equation for mrr and is used to compute the mrr at the ideal level of input parameters. The results are compared to the experimental data provided in Table 3.11.

Table 3.10. Optimum levels of input parameters for response.

Outcome	Factors	Level explanation	Levels
MRR	Feed (mm/rev.)	30	1
	Tool speed (RPM)	1490	2

Table 3.11. Calculated and experimental values at optimum level.

Outcome	Claculated	Experimental	%error
MRR	5.5178	6.5068	15

The maximum of 3.7% of errors are made.

$$MRR = -11.32 + 0.00904\ speed + 0.1676\ feed \quad (3.8)$$

The suitability of the model is determined to be adequate for further research. The conclusion from the analysis of variance in this study might be sent for additional analysis to forecast the optimum setting. When milling 3D printed FRT composites, it can improve the quality of the slot surface. As a result, the ANOVA model has been established in this work.

3.9.8 Response Optimization of the MRR of the hybrid Composites

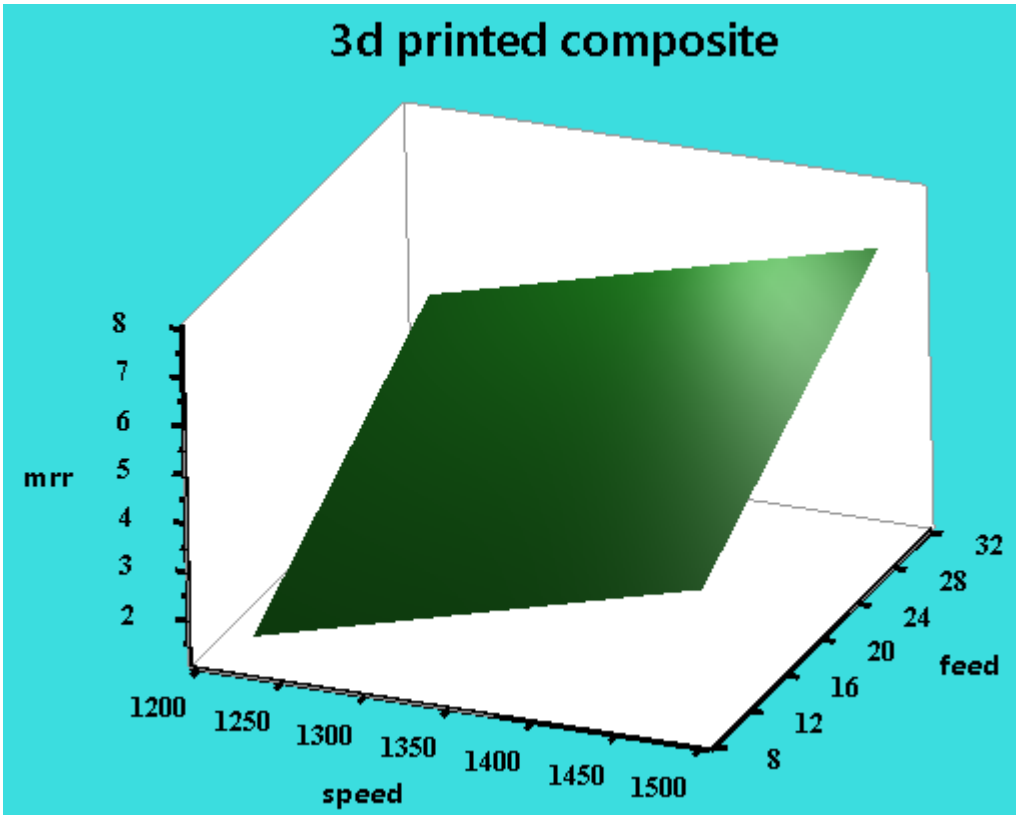

Figure 3.20. Surface Plot of MRR (mg/min) vs feed (rev/min), tool speed (RPM)

Utilizing contours and 3D plots of RSM, it was possible to assess the interactive relationship between the mix design factors and the properties of three different types of 3D printed composites sample such as continuous HSHTGF-FRT (0^0), K-FRT (0^0) and GFRT (0^0). Figure 3.20, Figure 3.21 and Figure 3.22 displays the surface plot, contour plot and interaction plot, respectively. Prior to getting the optimum response surface, Figure 3.22 was used to illustrate the relevance of the major influence of the independent components and their interaction on the outcome that can respond differently by the factors' different levels. As a result, if the outcome exhibits a parallel response to the x-axis, there is no main influence; its significance only becomes apparent when the response exhibits a slope behaviour. The magnitude of the major effect grows as this slope increases. The interaction plot illustrates how two separate factors can interact with one another and how this affects the outcome response. If parallel lines are used to represent the factors' impacts on response or duplicate behavior, this means there is no relationship, and hence, there is no interaction between the variables. Only when their curves' slopes vary does the interaction become visible and results in an intersection. In reality, The interaction effect increases as this variation rises [84].

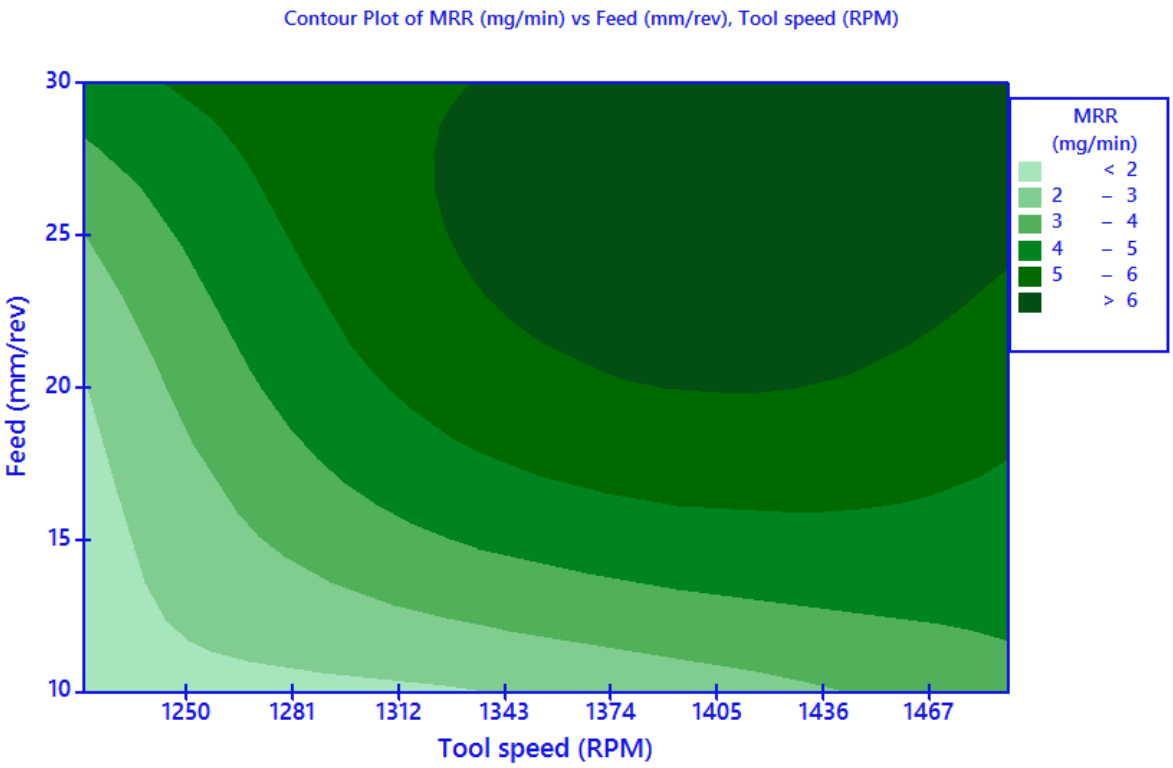

Figure 3.21. Contour Plot of mrr Vs Speed and Feed

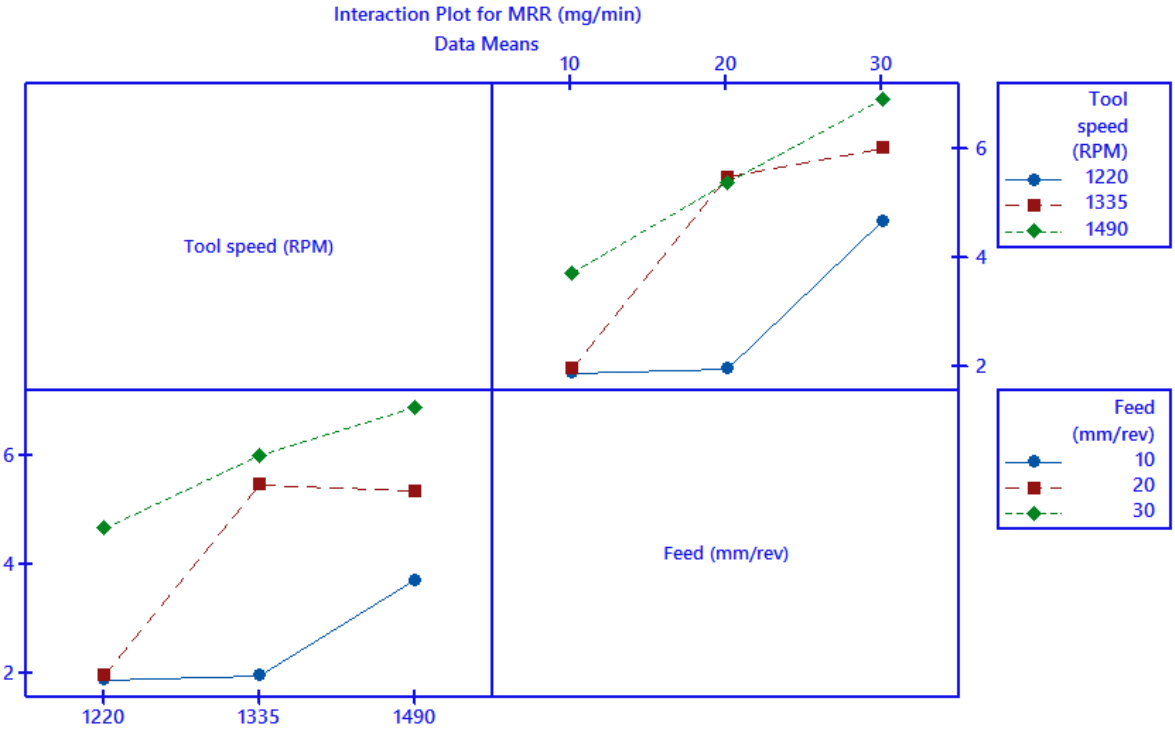

Figure 3.22. Interaction plot of MRR vs Speed and Feed

The impact of feed and tool rotational speed and their interaction effect on the material removal rate response of the hybrid composite has shown in Figure 3.22. Figure 3.22 shows that both factors significantly influenced the response. When compared to tool speed, the feed factor with a steeper slope has a bigger impact on the rate at which material is removed from the workpiece. But as the feed rate approached ten rev/min, this effect nearly disappeared, and a little upturn was seen as a result of the beginning of the phase transition in the epoxy matrix.

3.10 Fractography and Failure analysis

Figure 3.24, Figure 3.25, Figure 3.26 and Figure 3.27 are SEM micrographs of the three types of fiber-reinforced 3D printed composite sample. The fracture surfaces of the various fiber-reinforced composites were investigated using a scanning electron microscope (SEM) to determine the fibre pull out behaviour from the matrix. This depicts the bonding of the fibre and matrix interface; it is clear from the diagram that several types of failure occurred following destructive testing. The different types of failure are cohesive failure, adhesive failure, matrix debonding, fiber pulled out as can be observed in Figure 3.23, The pull-out behaviour of glass fibre is demonstrated; when the fibre separates from the matrix material, A little amount of matrix material is deposited on its surface. All those little matrix material deposition that was observed implies a somewhat excellent interface connection between the fibre and matrix, which implies a little amount of fibre from the matrix material slipping off during the tensile test. Figure 3.24 shows the fibre pull-out characteristic of Kevlar fibre from a 3D-printed polymer composite sample. The fibre pull-out from the matrix material has a smooth surface with very little matrix material deposition on the surface of the fibre.

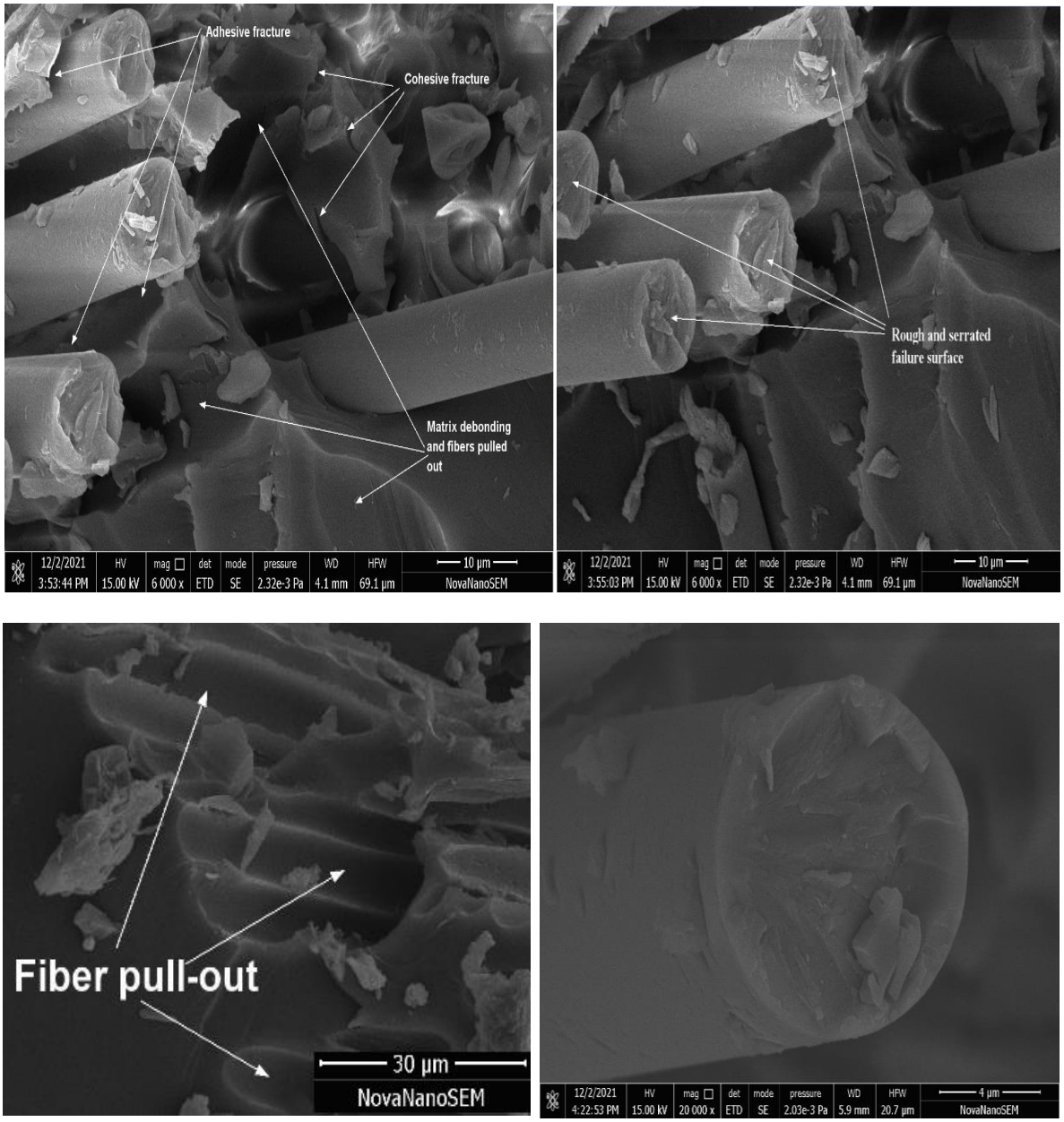

Figure 3.23. Comparison of morphology of different 3D printed composite specimen after quasi-static tensile test

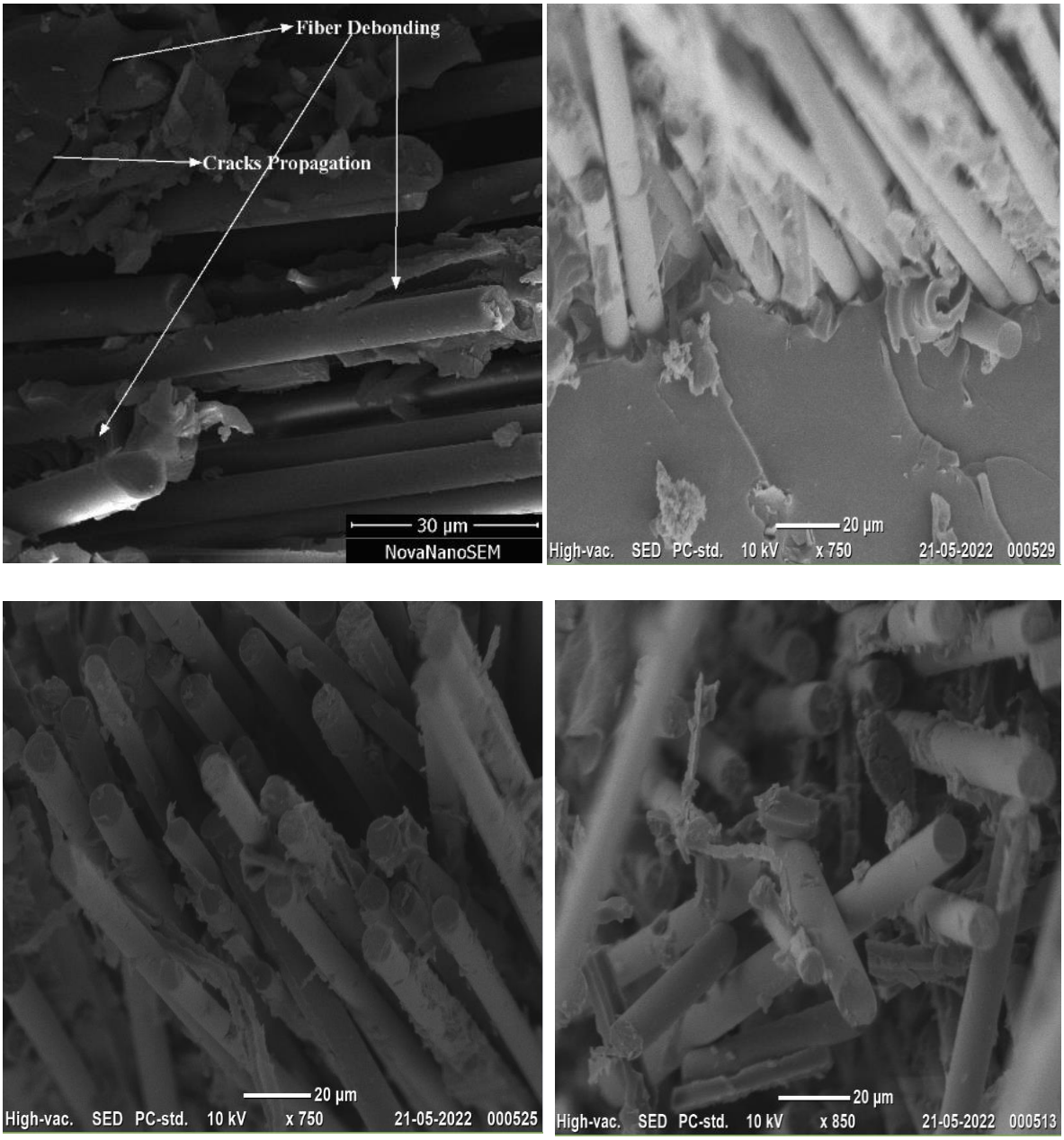

Figure 3.24. SEM image of impact fracture surface of different fiber reinforced 3D oriented composites.

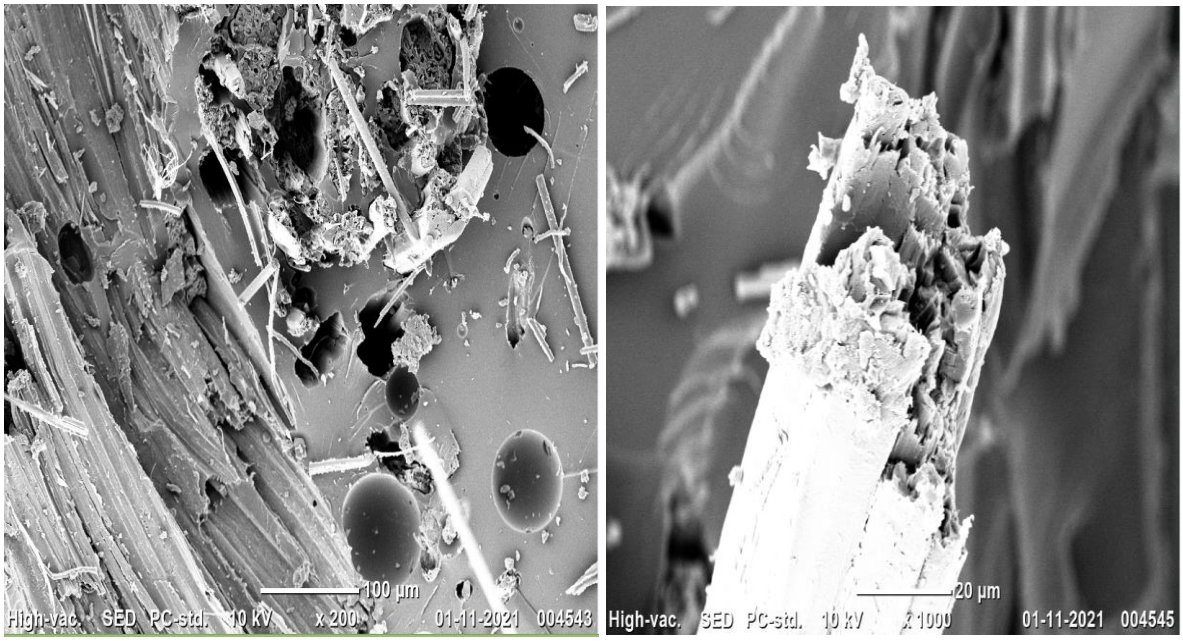

Figure 3.25. SEM micrograph of bending fracture surface of cross specimen

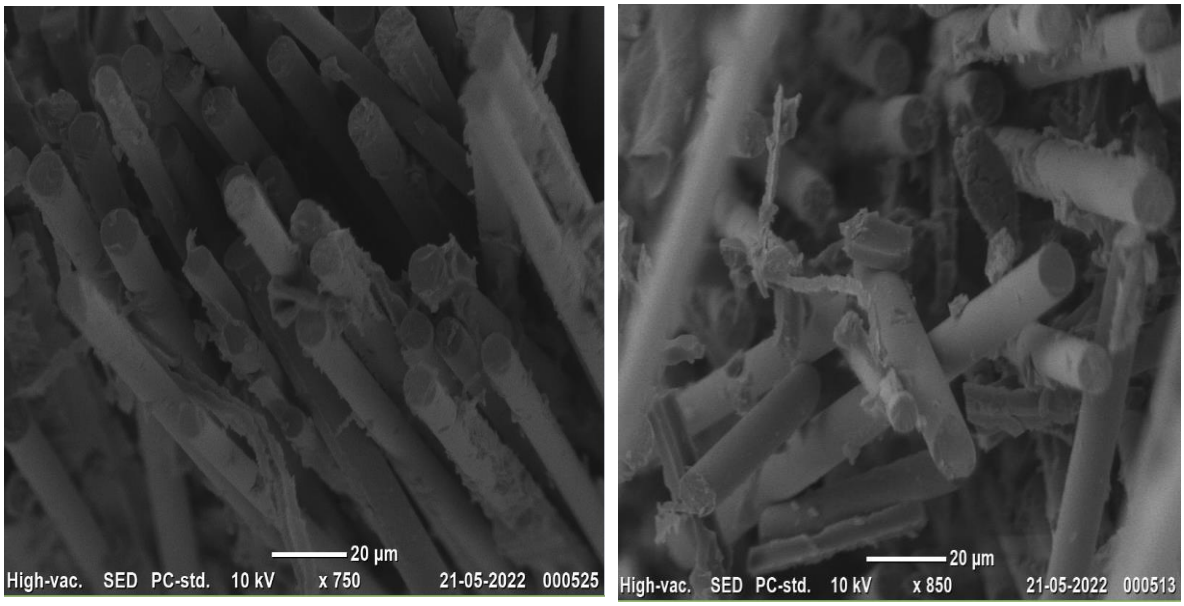

Figure 3.26. SEM image of fiber pull out from 3D printed composite specimen after impact fracture test.

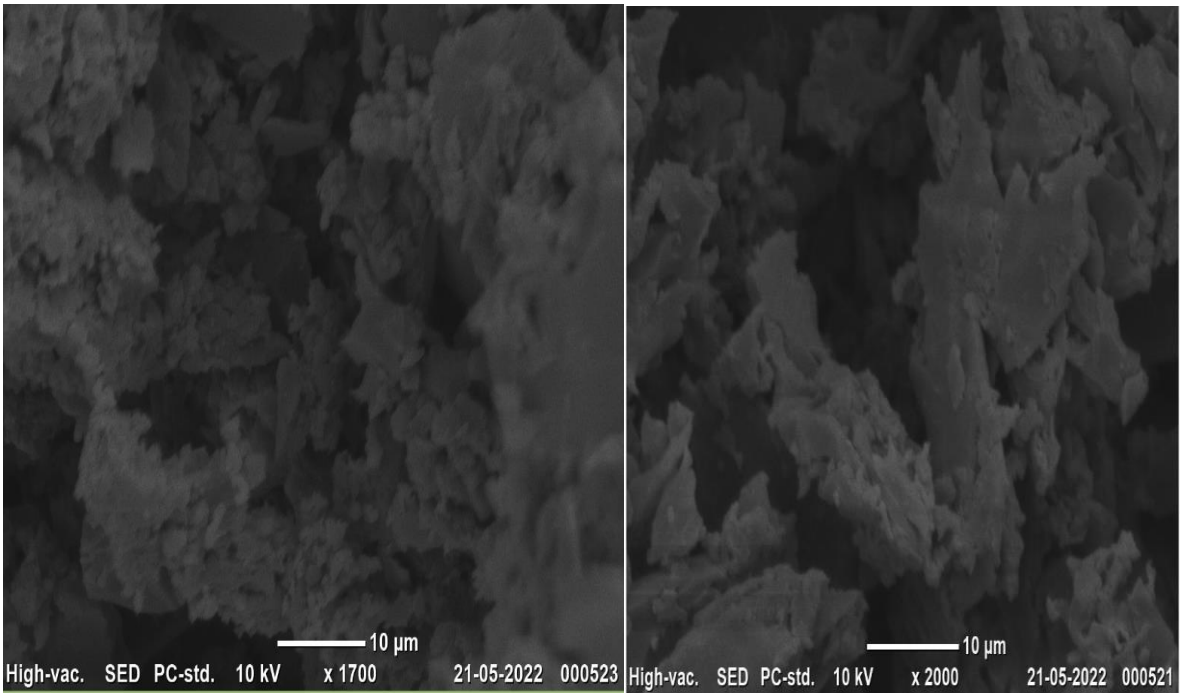

Figure 3.27. SEM image of the surface of HSHT glass fiber reinforced thermoplastic 3D printed composite after machining.

During izod impact testing, the fibres are easily pulled out of the matrix material, showing slippage of the fibre from the matrix and resulting in poor fibre and matrix interface bonding. This smooth surface is an indication of poor fibre and matrix interface bonding. Additionally, the creation and spread of cracks is readily apparent and results in failure. Figure 3.26 shows the fibre pull-out behaviour of HSHT glass fibre. The fibre pull away from the matrix material shows extra matrix material deposition on the surface of the fibre [84], and the observed more matrix material deposition on the surface of the fibre suggests a strong interface bonding of the fibre and matrix and implies nearly no slippage of fibre from matrix, which is consistent with prior research published [81]. Furthermore, the HSHT glass fibre reinforced 3D printed polymer composite is stiffer due to the strong interface bonding, which causes brittle fracture. As a result, it is clear from Figure 3.26 that, when compared to specimens

reinforced with glass and Kevlar fibres, HSHT glass fibre reinforced 3D printed polymer composite specimens had the strongest interface bonding. The figure illustrates how fibre pull-out impressions are more common than fracture impressions. Additionally, the fibres and matrix have been substantially deformed by the collision. Based on the analysis of the fracture surface, it seems like the material is flowing slowly. According to morphological study, the main reason composites fail is fibre breakage, which results from the composite's brittle nature.